



Electron Acceleration in the Heart of the Van Allen Radiation Belts

G. D. Reeves *et al.*

Science **341**, 991 (2013);

DOI: 10.1126/science.1237743

This copy is for your personal, non-commercial use only.

If you wish to distribute this article to others, you can order high-quality copies for your colleagues, clients, or customers by [clicking here](#).

Permission to republish or repurpose articles or portions of articles can be obtained by following the guidelines [here](#).

The following resources related to this article are available online at www.sciencemag.org (this information is current as of September 11, 2013):

Updated information and services, including high-resolution figures, can be found in the online version of this article at:

<http://www.sciencemag.org/content/341/6149/991.full.html>

Supporting Online Material can be found at:

<http://www.sciencemag.org/content/suppl/2013/07/24/science.1237743.DC1.html>

A list of selected additional articles on the Science Web sites **related to this article** can be found at:

<http://www.sciencemag.org/content/341/6149/991.full.html#related>

This article **cites 36 articles**, 1 of which can be accessed free:

<http://www.sciencemag.org/content/341/6149/991.full.html#ref-list-1>

Acknowledgments: The experimental work was supported by the Austrian Science Fund (FWF; project F45) and the European Research Council Advanced Grant "OxideSurfaces." The theoretical work was supported by the U.S. Department of Energy (DOE)—office of Basic Energy Sciences, Division of Chemical Sciences, Geosciences, and Biosciences under award DE-FG02-12ER16286. We used resources of the National Energy Research Scientific Computing Center (DOE contract

DE-AC02-05CH11231) and the Terascale Infrastructure for Groundbreaking Research in Science and Engineering High-Performance Computer Center at Princeton University.

Supplementary Materials

www.sciencemag.org/cgi/content/full/341/6149/988/DC1
Materials and Methods

Supplementary Text
Figs. S1 to S11
Tables S1 and S2
References (28–30)
Movies S1 and S2

30 April 2013; accepted 2 August 2013
10.1126/science.1239879

Electron Acceleration in the Heart of the Van Allen Radiation Belts

G. D. Reeves,^{1*} H. E. Spence,² M. G. Henderson,¹ S. K. Morley,¹ R. H. W. Friedel,¹ H. O. Funsten,¹ D. N. Baker,³ S. G. Kanekal,⁴ J. B. Blake,⁵ J. F. Fennell,⁵ S. G. Claudepierre,⁵ R. M. Thorne,⁶ D. L. Turner,⁷ C. A. Kletzing,⁸ W. S. Kurth,⁸ B. A. Larsen,¹ J. T. Niehof¹

The Van Allen radiation belts contain ultrarelativistic electrons trapped in Earth's magnetic field. Since their discovery in 1958, a fundamental unanswered question has been how electrons can be accelerated to such high energies. Two classes of processes have been proposed: transport and acceleration of electrons from a source population located outside the radiation belts (radial acceleration) or acceleration of lower-energy electrons to relativistic energies in situ in the heart of the radiation belts (local acceleration). We report measurements from NASA's Van Allen Radiation Belt Storm Probes that clearly distinguish between the two types of acceleration. The observed radial profiles of phase space density are characteristic of local acceleration in the heart of the radiation belts and are inconsistent with a predominantly radial acceleration process.

Radial diffusion of geomagnetically trapped electrons occurs continuously in Earth's time-varying magnetic field. Early theo-

ries of the formation of the Van Allen radiation belts focused on betatron and Fermi acceleration processes that act when electrons are transported from the outer magnetosphere where magnetic fields are weak (<100 nT) to the radiation belts, in the inner magnetosphere, where the magnetic fields are strong (*1, 2*). The single-point measurements and low time resolution of early satellite observations suggested that radial diffusion could generally explain the equilibrium structure of the radiation belts and its evolution on the longer time scales (days to weeks) revealed in early satellite observations. In the 1990s, a growing network of satellites provided multipoint measurements with temporal and spatial resolutions, revealing com-

plex structure and rapid dynamics that were difficult to explain with conventional theory.

In January 1997, a solar coronal mass ejection produced a strong geomagnetic storm and a dramatic intensification of radiation belt electron fluxes at energies up to several MeV (*3, 4*). Comparison of the dynamics at geosynchronous orbit [$\sim 6.6R_E$ (R_E is Earth's radius, 6372 km) or 42,000 km geocentric distance] and in the heart of the electron belt ($\sim 4.2R_E$ or 27,000 km) showed that the intensification of relativistic electron fluxes occurred first in the heart of the belts and on extremely rapid time scales (~ 12 hours) and only later and more slowly at higher altitudes. In contrast with radial diffusion theory, these observations strongly suggested an energization process operating locally in the heart of the radiation belts (*3*). A leading candidate for that process was proposed to be acceleration by resonant interactions between radiation belt electrons and naturally occurring electromagnetic very low frequency (VLF) ($\gtrsim 1$ kHz, i.e., radio) waves (*5–10*). However, around the same time other observations (*11*) showed a strong correlation between radiation belt electron enhancements and the power in global ultralow frequency (ULF) waves, which are enhanced during geomagnetic storms. Subsequent studies suggested that rapid enhancements of the radiation belts could be explained by acceleration from rapid, time-varying radial diffusion driven by the strong ULF field fluctuations (*12–17*).

Measurements of electron flux (electrons $\text{cm}^{-2} \text{s}^{-1} \text{sr}^{-1} \text{MeV}^{-1}$) cannot distinguish between local acceleration and acceleration by radial transport because both can produce radial peaks in electron flux. However, phase space density, which is the

¹Space Science and Applications Group, Los Alamos National Laboratory, Los Alamos, NM 87545, USA. ²Each Institute for the Study of Earth Oceans and Space, University of New Hampshire, Durham, NH 03824, USA. ³Laboratory for Atmospheric and Space Research, University of Colorado, Boulder, CO 80309, USA. ⁴NASA Goddard Space Flight Center, Greenbelt, MD 20771, USA. ⁵The Aerospace Corporation, El Segundo, CA 90245, USA. ⁶Department of Atmospheric and Ocean Sciences, University of California, Los Angeles, CA 90095, USA. ⁷Department of Earth and Space Sciences, University of California, Los Angeles, CA 90095, USA. ⁸Department of Physics, University of Iowa, Iowa City, IA 52242, USA.

*Corresponding author. E-mail: reeves@lanl.gov

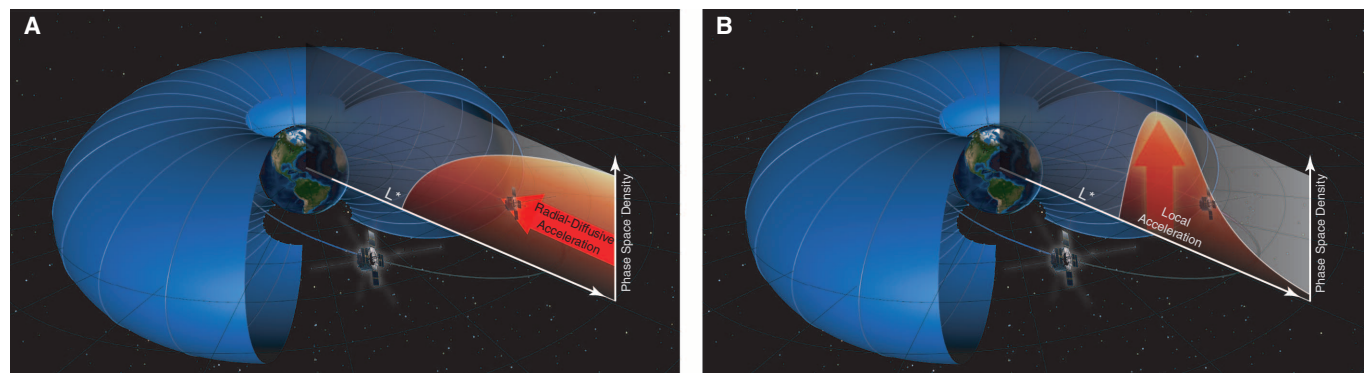


Fig. 1. The geometry of the radiation belts and RBSP orbits shown to scale. The positions of the RBSP satellites at 07:57 UT on 9 October are indicated. Also shown, in a cut-away view, is a single drift shell for electrons with 15° equatorial pitch angles starting at the position of RBSP-A at a radial

distance $L^* \approx 4.2$. Representative magnetic field lines are plotted in light blue between the northern and southern magnetic mirror points. The radial profiles of phase space density expected from radial-diffusive acceleration (**A**) and local wave-particle acceleration (**B**) are indicated schematically.

electron flux divided by the square of the momentum, does show unique signatures for local versus radial acceleration when expressed as a function of “magnetic coordinates.” NASA’s recently launched Van Allen Radiation Belt Storm Probes (RBSP) mission was designed to make the measurements needed to distinguish whether local or radial acceleration is the primary driver behind radiation belt electron acceleration events (18). Here, we report on the radial profiles of phase space density observed during the first major radiation belt enhancement event of the RBSP mission.

In Earth’s magnetic field, the motion of electrons is constrained to “drift shells” where electrons bounce between northern and southern magnetic mirror points and drift azimuthally around Earth (Fig. 1). To distinguish between local and radial acceleration, we must express phase space density not as it is measured—as a function of energy, pitch angle, and position—but rather as a function of the magnetic coordinates, μ , K , and L^* ,

that constrain electron motion (figs. S1 and S2). For radiation belt electrons, the quantity L^* defines their radial location, as measured from the center of Earth. Radial diffusion moves electrons in L^* while conserving the quantities μ and K . Because it is a stochastic process, diffusion moves electrons from regions of higher to lower phase space density. Therefore, enhanced radial diffusion from a source population at high L^* can increase the phase space density at lower L^* , but the gradients will still exhibit a monotonic decrease from the source or, equivalently, a monotonic increase with increasing L^* (Fig. 1A). In contrast, local acceleration processes keep an electron’s position (L^*) essentially constant while increasing its energy. Therefore, local acceleration processes produce increases in phase space density over a limited range of L^* , which, if sufficiently strong, will lead to a local peak in the radial profile with negative radial gradients at higher L^* (Fig. 1B).

Beginning with the January 1997 radiation belt electron event, studies have analyzed the radial profiles of phase space density and have provided growing evidence for local acceleration (4, 19–22). However, those studies were limited by a number of factors, including detector limitations, high backgrounds from penetrating radiation, poor energy coverage or resolution, limitations imposed by the satellite inclination or orbital period, and limited radial coverage (23). The RBSP mission was designed specifically to overcome those limitations by providing measurements near the magnetic equator, with broad and continuous energy coverage and rapid radial cuts through the heart of the radiation belts, and simultaneous measurements from spatially separated satellites (24). The two RBSP satellites were launched on 30 August 2012 into a near-equatorial, elliptical orbit with apogee at $5.7R_E$.

On 9 October 2012, the twin RBSP satellites measured an intense relativistic electron acceleration

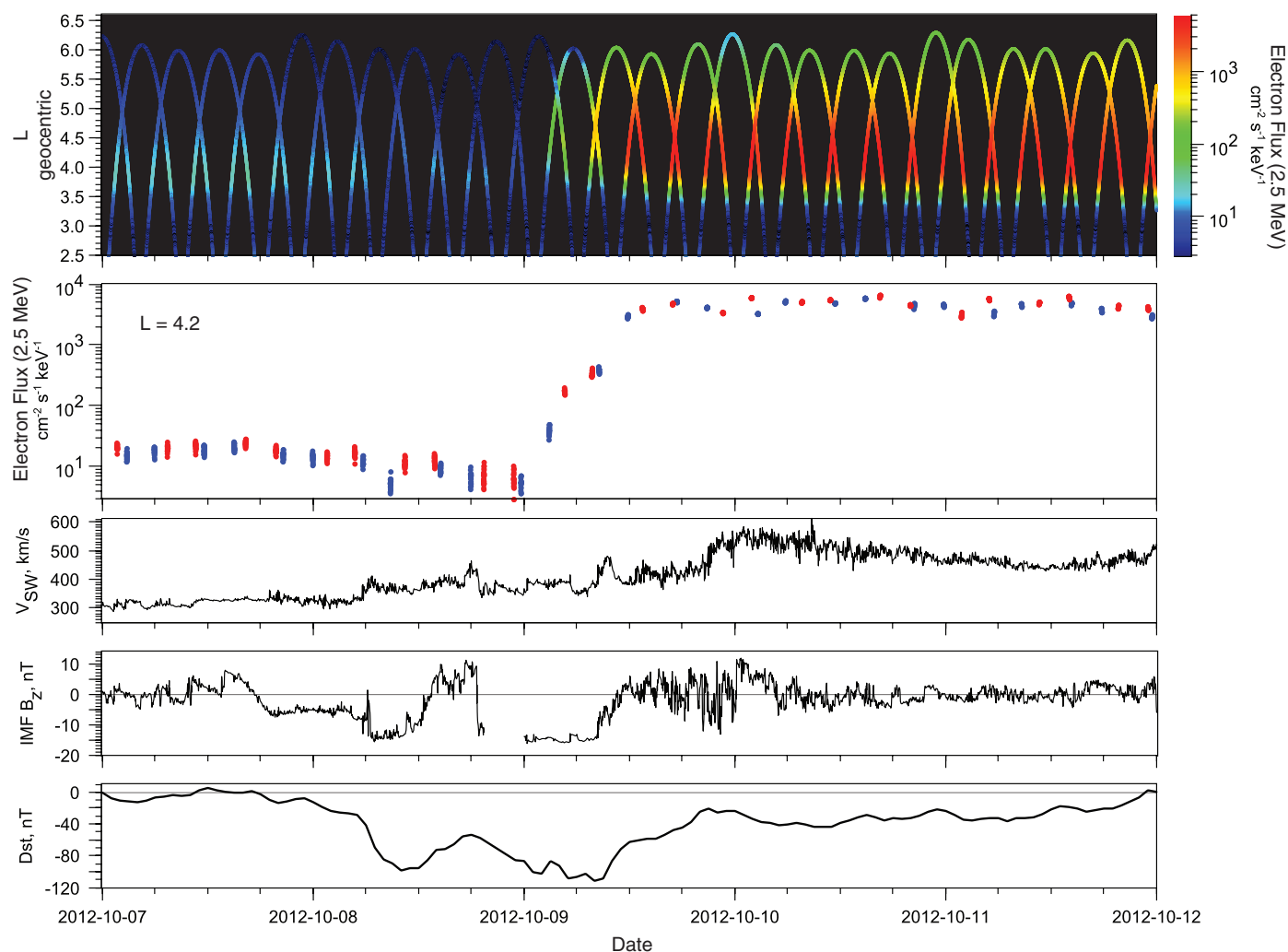


Fig. 2. An overview of the October 2012 geomagnetic storm and radiation belt electron event. The top graph shows the flux (intensity) of 2.5 MeV electrons from the MagEIS magnetic spectrometer (30) on NASA’s twin RBSP satellites. The second graph shows the fluxes at a radial distance of $L = 4.2$. The bottom three graphs show solar wind speed (V_{sw}), the

interplanetary magnetic field north-south component (IMF B_z), and the disturbance storm time index (Dst, a measure of geomagnetic storm intensity). The geomagnetic activity late on 8 October and into 9 October produced a very intense and very rapid increase in fluxes. More information on solar wind, geomagnetic, and VLF wave conditions is in the supplementary materials.

ation event (Fig. 2). Geomagnetic storms can either intensify or deplete the fluxes of MeV electrons in the outer belt (25). A storm on 1 October strongly depleted the outer electron belt (26), and electron fluxes remained exceptionally low and fairly constant until 8 October. The fluxes of outer belt electrons continued to gradually decrease until early on 9 October, when the fluxes of MeV electrons began to rapidly increase. In many radiation belt electron acceleration events, the fluxes

rise gradually over the course of a day or two. This event more closely resembles the January 1997 event in that the fluxes rose nearly three orders of magnitude in a period of less than 12 hours.

We plotted the time-dependent radial profiles of phase space density in order to look for the characteristic signatures of either radial or local acceleration (Fig. 3). In the first pass on 8 October (labeled 18:22), the RBSP-A spacecraft was out-bound starting at $L^* = 3.6$ at 17:32 UT, reaching

an apogee of $L^* = 5.2$ at 21:17 UT. Comparison with the subsequent profiles at 18:27 and 23:17 UT shows that there was little temporal evolution, and each pass can essentially be considered a snapshot of the phase space density profile.

Between the passes labeled 23:17 (8 October) and 03:32 UT (9 October), the radiation belts experienced a rapid increase in phase space density that continued for the next 10 hours. The increase in phase space density is most rapid in the heart of the radiation belts, in the vicinity of $L^* = 4.2$. In the early stages of the event, the phase space densities at higher L^* (e.g., 4.8) change only slightly to produce a pronounced peak in the radial profiles. In the passes labeled 4:12 and 7:57 UT, the radial peak in phase space density and the negative gradients at high L^* continue to grow. The pass labeled 3:32 UT is complicated because the magnetosphere was changing on time scales that are comparable to the transit of the RBSP-A satellite through the belt (figs. S6 and S7).

In the passes labeled 8:22 and 13:02 UT, the negative radial gradients at high L^* began to smooth out even as the peak phase space density increased, indicating that, in addition to local acceleration, radial diffusion also affected the radiation belt electrons by transporting them radially outward (and inward) from the newly formed peak. From 10:22 UT on 9 October through 12 October (labeled “late times”), the phase space density profiles show very little change, which is consistent with the abrupt decrease of energy input into the magnetosphere as the IMF turned northward (Fig. 2).

As noted in previous studies (18, 20, 22), single-satellite studies of phase space density gradients are subject to some spatial-temporal ambiguity because of the finite time for a single satellite to move from one L^* to another. By using simultaneous measurements of the phase space density measured at different L^* by the two RBSP satellites, we can further test whether instantaneous gradients are consistent with those seen in a finite-duration satellite pass. Starting at 05:57, RBSP-A was on the inbound leg of its orbit (labeled 7:57 in Fig. 3). RBSP-A measured a negative radial gradient with phase space densities that increased from 2.2×10^{-9} at $L^* = 4.9$ to 5.4×10^{-8} at $L^* = 4.2$. At about 07:22, RBSP-B entered the outer electron belt moving outward (orbit labeled 8:22 in Fig. 3). RBSP-B measured a positive radial gradient with phase space densities that increased from 1.6×10^{-12} at $L^* = 3.4$ to 6.5×10^{-8} at $L^* = 4.2$. Starting at 07:22, the two satellites were making simultaneous observations on opposite sides of the peak (Fig. 4). From 7:22 to 8:12 UT, RBSP-A moved inward from $L^* = 4.5$ to 4.1 and measured phase space densities went from 3.0×10^{-8} to 4.4×10^{-8} . Although this is on the order of the uncertainty in the measurements, the inward-directed gradients are a smooth continuation of the gradients measured earlier. The twin RBSP measurements confirm that the radial peak in phase space density is indeed a real spatial structure and not the result of spatial-temporal aliasing.

Fig. 3. Phase space density profiles for relativistic radiation belt electrons. Profiles were measured by the Relativistic Electron-Proton Telescope instrument (31) on 8 and 9 October. Phase space density, f , is in units of $(\text{c}/\text{cm MeV})^3$ where c is the speed of light. By plotting $f(L^*)$ at fixed magnetic invariants, $\mu = 3433 \text{ MeV/G}$, and $K = 0.11 R_E G^{1/2}$, we can plot both inbound and outbound portions of the orbit for each satellite on a common basis, vastly increasing the spatial and temporal resolution relative to previous observations. We used the TS04 magnetic field model to calculate the invariants (32). Curves for RBSP-A (squares) and RBSP-B (circles) are color-coded and labeled by the time at which each satellite crossed $L^* = 4.2$. The rapid increase in phase space density in the vicinity of $L^* = 4.2$ and the slower, more delayed increase at higher L^* produce signatures of local acceleration: a peak in phase space density with positive radial gradients at lower L^* and negative radial gradients at higher L^* . The average uncertainty on the calculation of phase space densities at fixed μ and K is a factor of 1.4, and the maximum uncertainty is a factor of 2 as discussed in the supplementary materials and figs. S8 and S9.

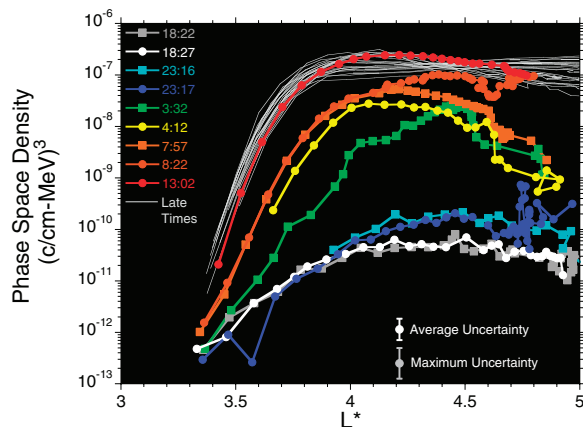
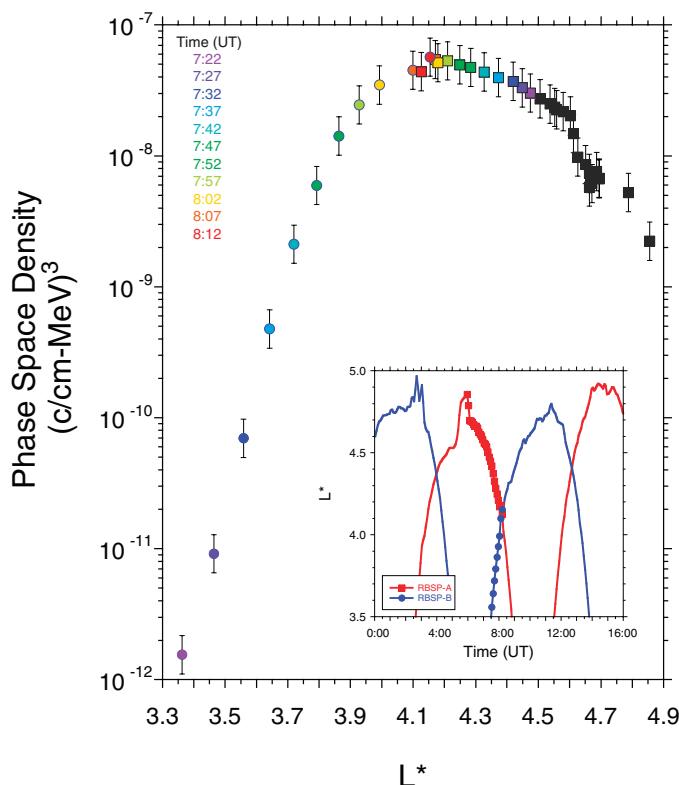


Fig. 4. Simultaneous measurements of phase space density from RBSP-A (squares) and RBSP-B (circles). Points are color-coded as a function of time when the two satellites were making simultaneous measurements of the radial gradients (07:22 to 08:12 UT). (Inset) The satellite orbits with RBSP-A inbound from apogee and RBSP-B outbound from perigee.



Numerical simulations (27) and other analyses (20) have shown that radial peaks in phase space density can in some cases be produced by radial diffusion in combination with a boundary condition at the outer edge of the belts that first increases to levels higher than the observed peak at lower L^* then decreases to levels below it. The shortness of the time between subsequent RBSP apogee passes provides stringent constraints on such a scenario but does not disprove it. Comparison between RBSP and geosynchronous phase space densities from five geosynchronous satellites that orbit outside RBSP's apogee and provide near-continuous monitoring of the outer boundary of the radiation belts confirms the negative radial gradient at high L^* , the lack of a potential source population at the outer boundary, and the necessity of an internal local acceleration process (fig. S10).

Although it is possible that radial acceleration may dominate in other relativistic acceleration electron events (28), the RBSP measurements of phase space density profiles on 8 and 9 October show signatures of local acceleration by wave-particle interactions in the heart of the radiation belts (29). The entire acceleration took place over a period of ≈ 11 hours between 23:17 UT on 8 October and 13:02 UT on 9 October. The primary acceleration was centered at $L^* \approx 4$ with evidence of acceleration observed between $L^* = 3.5$ to 4.5.

References and Notes

1. C. G. Fälthammar, *J. Geophys. Res.* **70**, 2503–2516 (1965).
2. M. Schulz, L. J. Lanzerotti, *Particle Diffusion in the Radiation Belts* (Springer-Verlag, New York, 1974).
3. G. D. Reeves *et al.*, *Geophys. Res. Lett.* **25**, 3265–3268 (1998).
4. R. S. Selesnick, J. B. Blake, *Geophys. Res. Lett.* **25**, 2553–2556 (1998).
5. A. D. M. Walker, *Plasma Waves in the Magnetosphere* (Springer-Verlag, New York, 1993).
6. D. Summers, R. M. Thorne, F. Xiao, *J. Geophys. Res.* **103**, 20487 (1998).
7. R. B. Horne, R. M. Thorne, *Geophys. Res. Lett.* **25**, 3011–3014 (1998).
8. I. Roth, M. Temerin, M. K. Hudson, *Ann. Geophys.* **17**, 631–638 (1999).
9. D. Summers *et al.*, *Geophys. Res. Lett.* **29**, 2174 (2002).
10. R. B. Horne *et al.*, *J. Geophys. Res.* **110**, A03225 (2005).
11. G. Rostoker, S. Skone, D. N. Baker, *Geophys. Res. Lett.* **25**, 3701–3704 (1998).
12. W. W. Liu, G. Rostoker, D. N. Baker, *J. Geophys. Res.* **104**, 17391–17407 (1999).
13. M. K. Hudson, S. R. Elkington, J. G. Lyon, M. Wiltberger, M. Lessard, *Space Weather* **125**, 289–296 (2001).
14. T. P. O'Brien, *J. Geophys. Res.* **108**, 1329 (2003).
15. S. R. Elkington, in *Magnetospheric ULF Waves: Synthesis and New Directions* [American Geophysical Union (AGU), Washington, DC, 2006], vol. 169, pp. 177–193.
16. A. Y. Ukhorskiy, B. J. Anderson, K. Takahashi, N. A. Tsyganenko, *Geophys. Res. Lett.* **33**, L06111 (2006).
17. R. A. Mathie, I. R. Mann, *Geophys. Res. Lett.* **27**, 3261–3264 (2000).
18. P. M. Kintner *et al.*, "The LWS geospace storm investigations: Exploring the extremes of space weather" (Living With A Star Geospace Mission Definition Team Report, NASA/TM-2002-211613, 2002).
19. N. P. Meredith, R. B. Horne, R. M. Thorne, R. R. Anderson, *Geophys. Res. Lett.* **30**, 1871 (2003).
20. J. C. Green, M. G. Kivelson, *J. Geophys. Res.* **109**, A03213 (2004).
21. R. H. A. Iles, N. P. Meredith, A. N. Fazakerley, R. B. Horne, *J. Geophys. Res.* **111**, A03204 (2006).

22. Y. Chen, G. D. Reeves, R. H. W. Friedel, *Nat. Phys.* **3**, 614–617 (2007).
23. Y. Y. Shprits, D. A. Subbotin, N. P. Meredith, S. M. Elkington, *J. Atmos. Sol. Terr. Phys.* **70**, 1694–1713 (2008).
24. B. H. Mauk *et al.*, *Space Sci. Rev.*, published online 7 September 2012 (10.1007/s11214-012-9908-y).
25. G. D. Reeves, K. L. McAdams, R. H. W. Friedel, T. P. O'Brien, *Geophys. Res. Lett.* **30**, 1529 (2003).
26. D. N. Baker *et al.*, *Science* **340**, 186–190 (2013); 10.1126/science.1233518.
27. R. S. Selesnick, J. B. Blake, *J. Geophys. Res.* **105**, 2607–2624 (2000).
28. J. F. Fennell, J. L. Roeder, *J. Atmos. Sol. Terr. Phys.* **70**, 1760–1773 (2008).
29. We note that at lower values of μ , corresponding to electrons in the 10s- to 100s-keV energy range, the dynamics are dominated by processes such as enhanced convection and substorm injections that are important precursors to relativistic (MeV) electron enhancements.
30. J. B. Blake *et al.*, *Space Sci. Rev.*, published online 7 June 2013 (10.1007/s11214-013-9991-8).
31. D. N. Baker *et al.*, *Space Sci. Rev.*, published online December 2012 (10.1007/s11214-012-9950-9).
32. N. A. Tsyganenko, M. I. Sitnov, *J. Geophys. Res.* **110**, A03208 (2005).

Acknowledgments: This work was supported by RBSP-Energetic Particle, Composition, and Thermal Plasma funding under NASA's Prime contract no. NAS5-01072. All Van Allen Probes (RBSP) observations used in this study, along with display and analysis software, are publicly available at the Web site www.rbsec-lanl.gov.

Supplementary Materials

www.sciencemag.org/cgi/content/full/science.1237743/DC1
Supplementary Text
Figs. S1 to S10
References (33–44)

12 March 2013; accepted 10 July 2013
Published online 25 July 2013;
10.1126/science.1237743

A Uranian Trojan and the Frequency of Temporary Giant-Planet Co-Orbitals

Mike Alexandersen,^{1*} Brett Gladman,¹ Sarah Greenstreet,¹ J. J. Kavelaars,² Jean-Marc Petit,³ Stephen Gwyn²

Trojan objects share a planet's orbit, never straying far from the triangular Lagrangian points, 60° ahead of (L4) or behind (L5) the planet. We report the detection of a Uranian Trojan; in our numerical integrations, 2011 QF₉₉ oscillates around the Uranian L4 Lagrange point for >70,000 years and remains co-orbital for ~ 1 million years before becoming a Centaur. We constructed a Centaur model, supplied from the transneptunian region, to estimate temporary co-orbital capture frequency and duration (to a factor of 2 accuracy), finding that at any time 0.4 and 2.8% of the population will be Uranian and Neptunian co-orbitals, respectively. The co-orbital fraction ($\sim 2.4\%$) among Centaurs in the International Astronomical Union Minor Planet Centre database is thus as expected under transneptunian supply.

During 2011 and 2012, we used the Canada-France-Hawaii Telescope to perform a 20-square-degree survey designed to de-

tect trans-Neptunian objects (TNOs) and objects between the giant planets with apparent r-band magnitude $m_r < 24.5$ and track all detections for up to 17 months. The project was accurately calibrated (I) to constrain the size and orbital parameter distributions of populations resonant with Neptune. Constraining the distribution of these populations is essential, as they in turn set constraints on models of the evolution of the outer solar system.

As part of this survey, we detected 2011 QF₉₉ (2) at a heliocentric distance of 20.3 astronomical units (AU), where its apparent magnitude $m_r = 22.6 \pm 0.1$ sets its absolute magnitude at $H_r = 9.6$ ($H_g = 10.3$, assuming a typical color $g - r \approx 0.7$). This magnitude indicates that 2011 QF₉₉ is ~ 60 km in diameter, assuming a 5% albedo. As more observations constrained the orbit, it became clear that 2011 QF₉₉ was not simply a Centaur that happened to be near the distance of Uranus. Our current astrometry, consisting of 29 measurements from seven dark runs with a total arc of 419 days, indicates the following orbital elements: $a = 19.090 \pm 0.004$ AU, $e = 0.1765 \pm 0.0007$, $i = 10.811^\circ \pm 0.001^\circ$, $\Omega = 222.498^\circ \pm 0.001^\circ$, $\omega = 287.51^\circ \pm 0.11^\circ$, and $T = 246\,4388 \pm 11$ JD. Here, a , e , i , Ω , ω , T are the osculating J2000 barycentric semimajor axis, eccentricity, inclination, longitude of ascending node, argument of pericenter, and Julian day of pericenter. The low eccentricity along with a semimajor axis similar to that of Uranus ($a_U \approx 19.2$ AU) indicated that 2011 QF₉₉ might be a Uranian co-orbital. Co-orbital bodies are in the 1:1 mean-motion resonance with a planet (thus having the same orbital period) and a librating (oscillating) resonant angle $\phi_{11} = \lambda - \lambda_{\text{Planet}}$. Here, λ is the mean longitude, which is the sum of Ω , ω , and the mean anomaly. ϕ_{11} roughly measures how far ahead in orbital phase the object

¹Department of Physics and Astronomy, University of British Columbia, 6224 Agricultural Road, Vancouver, BC V6T 1Z1, Canada. ²National Research Council of Canada, Victoria, BC V9E 2E7, Canada. ³Institut UTINAM, CNRS-UMR 6213, Observatoire de Besançon, BP 1615, 25010 Besançon Cedex, France.

*Corresponding author. E-mail: mikea@astro.ubc.ca



Supplementary Materials for

Electron Acceleration in the Heart of the Van Allen Radiation Belts

G. D. Reeves,* H. E. Spence, M. G. Henderson, S. K. Morley, R. H. W. Friedel, H. O. Funsten, D. N. Baker, S. G. Kanekal, J. B. Blake, J. F. Fennell, S. G. Claudepierre, R. M. Thorne, D. L. Turner, C. A. Kletzing, W. S. Kurth, B. A. Larsen, J. T. Niehof

*Corresponding author. E-mail: reeves@lanl.gov

Published 25 July 2013 on *Science Express*
DOI: 10.1126/science.1237743

This PDF file includes:

Supplementary Text
Figs. S1 to S10
References

Supplementary Materials for

Electron Acceleration in the Heart of the Van Allen Radiation Belts

G. D. Reeves, H. E. Spence, M. G. Henderson, S. K. Morley, R. H. W. Friedel, H. O. Funsten, D. N. Baker, S. G. Kanekal, J. B. Blake, J. F. Fennell, S. G. Claudepierre, R. M. Thorne, D. L. Turner, C. A. Kletzing, W. S. Kurth, B. A. Larsen, and J. T. Niehof

correspondence to: reeves@lanl.gov

This file includes:

SupplementaryText
Figs. S1 to S10

Supplementary Text:

Solar Wind and Geomagnetic Activity

Relativistic electron acceleration is the result of a series of processes that begin with transfer of energy from the solar wind into the magnetosphere. Two of the important solar wind parameters that determine energy transfer are the interplanetary magnetic field (IMF) and the solar wind speed (V_{sw}). Southward IMF ($B_z < 0$) enables reconnection with the Earth's magnetic field that efficiently transfers energy into the magnetosphere. This can produce geomagnetic storms which inject moderate energy (10s to 100s keV) electrons and ions into the inner magnetosphere where they build up the ring current, provide a source of free energy for electromagnetic waves, and provide a seed population that can subsequently be accelerated to higher energies. The Disturbance storm time (Dst) index is a measure of geomagnetic storm activity. $Dst < -50$ nT and < -100 nT represent moderate and strong storm activity respectively.

Late on October 7 the interplanetary magnetic field (IMF) turned moderately southward. It became more strongly southward on October 8 driving moderate to strong storm activity. At the same time the outer belt electron fluxes began to decrease slightly. Following a partial weakening of storm activity and a brief northward turning, the IMF turned rapidly and strongly southward again and storm activity re-intensified. The onset of the increase in relativistic outer belt electron fluxes is the result of processes that began earlier but the rapid changes observed here cannot easily be associated with the timing of any particular solar wind drivers. High solar wind speed ($V_{sw} \approx 500$) is often correlated with radiation belt intensifications (32) but, in this event, the solar wind speed was only slightly faster than average and did not reach speeds of > 500 km/s until well after the acceleration was over. In contrast, the end of the acceleration event corresponds closely with the northward turning of the IMF and the recovery of Dst. Thereafter the IMF fluctuated around zero and the outer belt fluxes remained fairly constant.

Electron Motion and Adiabatic Invariants

Electron motion in a steady-state dipole-like magnetic field can be described by three periodic motions - gyration around the magnetic field, bounce along the magnetic field between magnetic mirror points, and azimuthal gradient-curvature drift around the

magnetosphere. Each has an associated “magnetic invariant” which is approximately conserved under adiabatic changes to the magnetic field. The time scales associated with gyration, bounce, and drift are milliseconds, seconds, and tens of minutes respectively. The first invariant, μ , is associated with the gyro-motion around the magnetic field and is given by

$$\mu = \frac{p_{\perp}^2}{2m_0 B}$$

where m_0 is the rest mass, and p_{\perp} is the relativistic momentum in the direction perpendicular to the magnetic field, B .

When μ is approximately conserved, the motion of an electron can be described by guiding center theory (33) which describes the motion of the electron’s gyro-center neglecting circular motion around the gyro-center. The guiding-center motion of an electron is described by a “drift-shell” that resembles a section of the outer surface of a toroid. The bounce motion along a magnetic field line is constrained by the magnetic mirror points that, in turn are defined by the electron’s pitch angle

$$\alpha = \tan^{-1} \frac{p_{\perp}}{p_{\parallel}}$$

where, again the perpendicular and parallel directions are with respect to the magnetic field. Electrons with a 90° equatorial pitch angle mirror at the geomagnetic equator. More field-aligned electrons ($\alpha \rightarrow 0^\circ, \alpha \rightarrow 180^\circ$) mirror further and further from the magnetic equator. The invariant associated with the bounce motion between the Northern and Southern mirror points is

$$J = \oint p_{\parallel} ds = 2 \int_{s_s}^{s_n} p_{\parallel} ds$$

which, when μ is conserved can also be expressed as the energy-independent invariant

$$K = \frac{J}{2\sqrt{2m_0\mu}} = \int_{s_s}^{s_n} \sqrt{B_m - B(s)} ds$$

where B_m is the magnetic field strength at the mirror point and s is the path length along the field line. The third invariant is an integral around the drift shell and between the mirror points

$$\Phi = \oint \vec{B} \cdot d\vec{A}$$

which conserves the total magnetic flux enclosed within a drift shell. In radiation belt physics it is more common to use the L^* parameter (34)

$$L^* = \frac{2\pi M}{\Phi R_E}$$

where, M is the Earth’s magnetic moment and R_E is the radius of the Earth (6,370 km).

The parameter L is defined as the geocentric distance at which a given magnetic field line crosses the equator. In a dipole magnetic field $L^* = L$. However, in a realistic geomagnetic field, the L^* for a fixed point in space changes as the field changes. In general, L^* for a fixed measurement point decreases with increasing geomagnetic activity - a feature known as the “Dst effect” (35). Since (in the absence of acceleration or loss) L^* defines a surface of constant phase space density it is the appropriate parameter for

those purposes. However, when plotting electron flux at constant energy, which is not a conserved quantity, it is more appropriate to use the parameter L (as we do in figure 2).

Phase Space Density Measurements

The RBSP mission was designed to overcome the limitations preventing previous satellite observations from resolving the controversy surrounding local vs. radial acceleration (18). The satellite orbit must traverse the radiation belts but it also needs to be near the geomagnetic equator. Radial and local acceleration affect the equatorial pitch angle distribution of electrons differently. Radial acceleration most strongly affects 90° (equatorially-mirroring) electrons. Satellite observations far off the magnetic equator can only measure the more field-aligned part of the population and can therefore miss some of the effects of radial acceleration. Since phase space density must be calculated at constant K it is the minimum K value at the point furthest off the equator that determines which equatorial can be observed throughout the orbit – i.e. at all measured L^* .

Pitch-angle resolved measurements are needed to calculate phase space density as a function of K at any point along the orbit. Many satellite measurements use omnidirectional or hemispherical detectors that cannot resolve pitch angle. In those cases, assumptions about the pitch angle distributions and their time-dependence adds ambiguity to phase space density values. Similarly, since the magnetic field changes with position, the requirement to calculate phase space density at constant μ implies that measurements must span a broad range of energies and must also have sufficient energy resolution.

We have already noted possible effects of spatial-temporal ambiguity inherent in single satellite measurements. As also noted in previous studies (20, 22) peaks in phase space density can be produced by radial diffusion without local acceleration if the source population at high L^* values decreases rapidly after the initial acceleration. Significant gaps in either time or L^* can allow some ambiguity in the interpretation. The ideal case would be to have continuous measurements at all L^* simultaneously. Since this is not possible with a finite number of satellites the best compromise is to have simultaneous multi-point measurements with sufficiently rapid radial motion that the coverage is continuous on the time scales of interest which is the case for the RBSP measurements.

The RBSP satellites are capable of measuring phase space density over a much broader range of μ , K , and L^* than any previous observations. In transforming from flux to phase space density we first pick a fixed set of μ and K and for each L^* along a satellite orbit. We then determine the energy and pitch angle of the electrons that correspond to that μ and K . To obtain statistically significant pitch angle distributions at these high energies we average the RBSP data in 5 min bins along the orbit. We use interpolation in the measured spectrum and pitch angle distribution in order to have a continuous transformation function but we do not extrapolate beyond measured values.

Coverage in μ and K

We calculate μ and K along the satellite orbit using the TS04 magnetic field model. Figure S1 shows the relationship between μ and Energy along the RBSP-A orbit for October 8 and Figure S2 shows the relationship between K and the corresponding equatorial pitch angle. (The values for RBSP-A and -B for a given day are quite similar.) We chose a value of $\mu = 3433$ MeV/G to select energies that optimize L^* coverage

without getting too close to the upper or lower ends of the REPT instrument energy coverage (30). We applied similar conditions in our choice of K . Since we do not extrapolate the measured pitch angle distribution, we cannot calculate phase space density for all K at all L^* . The value $K = 0.11 R_E G^{1/2}$ provides coverage over a quite broad range of L^* while still constraining the corresponding equatorial phase space density to approximately 45° - 90° .

Electron Dynamics at Lower Energies

Although a full analysis of the evolution of radial profiles of phase space density for all values of μ and K is beyond the scope of this paper some general characteristics are worth noting. The RBSP measurements show a peak in phase space density developing in the heart of the belts for μ values upward of at least 1000 MeV/G and negative radial gradients at high L^* are observed for the same range. The beginning of the increase and the rate of increase in phase space density are both functions of μ consistent with acceleration of the electrons from lower to higher energies over a finite time. At lower values, $\mu < 1000$ MeV/G, the REPT measurements do not extend out to apogee. However, preliminary analysis of data from the THEMIS satellites suggests that below $\mu < 500$ MeV/G the radial gradient at high L^* transitions from negative to positive (figure S3). This is due to the fact that electrons with energies less than a few hundred keV are energized primarily by the electric fields associated with storm and substorm activity.

Wave-Particle Acceleration Processes

In order to accelerate relativistic electrons locally, in the heart of the radiation belts, the acceleration process must break the first adiabatic invariant. Field-line curvature scattering breaks the first invariant but does not provide additional energy. Wave-particle interactions are the only process known to operate in the magnetosphere that are capable of energizing electrons by MeVs. Since wave-particle interactions must operate on gyro-period time scales this puts the waves in the VLF frequency range (i.e. ≥ 1 kHz). Therefore we can conclude that the local acceleration observed in the heart of the radiation belts on October 8-9, 2012 was caused by resonant interaction with VLF waves but we cannot establish, based on current analysis, which specific VLF waves are responsible. Theory, modeling, and observations (36-38) suggest that the wave mode that is likely most effective for relativistic electron acceleration is VLF whistler-mode chorus waves. Figure S4 shows that intense chorus emissions were indeed observed in the region where local acceleration was observed providing evidence that is consistent with those theories.

Dependence on the Magnetic Field Model

Calculation of the second and third invariants (K , L^*) requires knowledge of the large-scale magnetic field that cannot be obtained from local satellite measurements and must be calculated from a global magnetic field model. There are several magnetic field models in common use. Most are based on fits to statistical measurements of the global magnetic field using different parameterizations and internal mathematical representations of the field. The Olsen-Pfitzer quiet (OP77Q) magnetic field model is a static (not time dependent) model which captures the general morphology of the average field (39). The T89 model (40) parameterizes the field with the geomagnetic index K_p .

We define a “quiet” version in which K_p is fixed at a value of 2 and a “dynamic” version that uses the measured value of K_p . The dynamic version captures some of the changes in the field (35) but, since K_p has a 3-hour resolution and has discrete values this introduces discontinuities. The TS04 model is a dynamic model that uses geomagnetic and solar wind parameters to produce a set of parameterization functions that are continuous in time (31). The TS04 is the model that is most likely to capture the dynamics of the true geomagnetic field.

Since the value of phase space density, f , depends on the values of μ , K and L^* which, in turn, depend on the magnetic field model, there is an inherent uncertainty in f that is introduced by the choice of magnetic field model (figure S5). However, as with previous studies (20) we find that, while the choice of field model has a significant effect on the value of L^* as a function of time, it has a rather small effect on the calculated values of μ and K .

As we have noted, the geomagnetic field was most dynamic and most likely to be poorly-represented by any magnetic field model during the time 2:30 to 6:00 UT on October 9 when the RBSP-A satellite was on an outbound traverse of the radiation belt. This pass, labeled 3:32 in figure 3, is reproduced in figure S6 which additionally plots the phase space density as a function of time. Although $f(L^*)$ shows considerable change in slope during this time $f(t)$ is considerably smoother indicating that it is the calculated value of $L^*(t)$ that is distorting the radial profiles. Irrespective of the calculation of L^* or the choice of field model, RBSP-A measures increasing phase space density as a function of time as it is outbound from 2:30 to approximately 4:30. As the satellite continues to move outbound toward apogee (e.g. 4:30 to 6:00) it measures decreasing phase space density and therefore a negative radial gradient.

Finally, for completeness, we plot phase space density as a function of spatial position which is also independent of the field model-based calculation of L^* . In figure S7 we plot phase space density as a function of geocentric radial distance, $f(R)$ for the inbound pass of RBSP-B labeled with the time 04:12 UT in figure 3. While $f(R)$ is not a conserved quantity, it still accurately represents the radial gradients when the phase space densities are changing more slowly than the duration of the pass (~3 hours). We also note that the thermal plasma populations that provide the free energy for wave growth do not conserve L^* and are dependent on the spatial coordinates R and magnetic local time (MLT). So, $f(R, \text{MLT})$ may be an important quantity in determining where wave-particle acceleration is most effective. Additionally, plotting $f(R)$ allows us to put the phase space densities into a spatial representation on the same scale as the RBSP orbits and the electron drift shells, as in figure S7.

Calculation of Uncertainties

As discussed above, the calculation of adiabatic invariants relies on the use of a global magnetic field models. Therefore an inaccuracy in the calculation of one or more of the invariants can lead to choosing the wrong phase space density out of the magnetic invariant parameter space. There are several ways that we can assess the potential effects of magnetic field inaccuracies on phase space density calculations.

To begin, in figure S8, we plot the observed magnetic field magnitude as a function of the model magnetic field magnitude along with the distribution of relative errors

$(B_{\text{observed}} - B_{\text{model}})/B_{\text{observed}}$. The standard error of the distribution is 4% and the maximum error is $\pm 15\%$. These uncertainties translate directly to uncertainties in μ and therefore to uncertainties in the energy to use for a fixed value of μ . The effect on uncertainties in electron flux (and therefore phase space density) are dependent on the energy spectrum, however, using the measured REPT spectrum the uncertainty in phase space density corresponding to a 15% uncertainty in B is less than a factor of 2. A standard error of 4% corresponds to a factor of 1.4. In figure 3 we refer to these values as the average and maximum uncertainty respectively. Both values are considerably smaller than the radial gradients in phase space density.

Uncertainties in the magnitude of B do not capture all of the potential factors that can affect the uncertainties in phase space density. Fortunately, with two satellites in the proper orbits, a technique called phase space density matching (41, 42) provides a direct way to measure those uncertainties that capture the collective effects of all potential uncertainties in the magnetic invariants as well as uncertainties due to possible cross-calibration errors in the instruments. Since phase space density is conserved along a drift shell, $f(\mu, K, L^*)$ measured simultaneously at two points on the drift shell should be identical. Errors in μ , K , L^* , or instrument response functions will show up as a difference. The two Van Allen Probes satellites provide numerous “drift shell conjunctions” where the satellites are at two different longitudes (and magnetic local times) but still measure the same drift shell at the same time (as calculated from the magnetic field model). In figure S9 we plot the phase space density difference factor for all the drift shell conjunctions on October 8-9 when the satellites were simultaneously measuring the same drift shell ($L^* \pm 0.1$). We find remarkable consistency with the uncertainties obtained from magnetic field magnitudes alone with most values matching within a factor of 1.4x and all values matching to better than a factor of 2.

Local Peaks and Outer Boundary Dynamics

Numerical simulations have shown that phase space density peaks can also be produced by a time-dependent outer boundary condition (27). Peaks can be produced by the following scenario: (a) at a certain time phase space density increases in the outer region of the radiation belts through substorm injections, convection, or other processes; (b) the electrons diffuse inward increasing the phase space density throughout the outer zone, i.e. from the outer boundary to the slot region; (c) at a later time the phase space density at the outer boundary decreases due to some electron loss process; (d) since it takes a finite time for electrons near the heart of the belts to diffuse inward to the slot or out to the outer boundary, a radial peak in phase space density may be formed.

The RBSP observations strongly constrain such a scenario for the October 8-9 event. Figure 3 shows that the phase space densities at the highest L^* 's increase or stay approximately constant from one pass to another. Since the satellites are roughly 180° out of phase in their orbital periods in October, 2012, there is a “gap” of 4.5 hours or less (particularly considering the relatively slow motion at apogee). Therefore the rate of radial diffusion and the increase/decrease of phase space density at the boundary would have to be both large and extremely rapid in order to produce the observed radial profiles, but, the RBSP observations alone cannot definitively rule out that possibility.

Fortunately, for the October 2012 event, we can also examine direct measurements of the outer boundary conditions using geosynchronous satellite observations. During this

interval, Los Alamos National Laboratory (LANL) operated instruments on five geosynchronous satellites distributed in longitude around the globe providing nearly continuous monitoring at all magnetic local times at a radial distance of $6.6 R_E$, $0.9 R_E$ beyond the RBSP apogee. The geosynchronous satellites do not carry magnetometers so the symmetry axis of the particle distributions is used to determine the magnetic field direction and subsequently to calculate the pitch angle distributions and phase space densities (22, 42).

In figure S10 we plot the phase space densities (for $\mu=3433$ MeV/G, $K=0.11 R_E G^{1/2}$) at geosynchronous orbit and in the heart of the radiation belts. Both are plotted as a function of time regardless of L^* . For RBSP we plot only points with $L^* > 3.8$. For geosynchronous orbit the L^* at a given time can be different for different satellites due to the asymmetries in the geomagnetic field. Additionally, the variation in L^* with geomagnetic activity generally increases with increasing radial distance (and decreasing geomagnetic field strengths). When plotted as a function of time, rather than L^* , changes in phase space densities are a combination of adiabatic and non-adiabatic effects. Nevertheless, given the near-equatorial positions of all seven satellites, geosynchronous orbit is always at an L^* that is larger than or nearly equal to the L^* of RBSP. During October 8-9 there are a few brief intervals (e.g. $\sim 09:00$ on October 8 and $\sim 00:00$ to $\sim 06:00$ on October 9) when the L^* of one of the geosynchronous satellites is nearly equal to the L^* of one of the RBSP satellites and, at those times, the phase space densities are quite comparable, as expected. The remainder of the time $L^*_{GEO} > L^*_{RBSP}$ and $PSD_{GEO} < PSD_{RBSP}$ indicating a strong negative radial gradient at the outer edge of the radiation belts. These observations rule out the possibility that the peaks of phase space density observed in the heart of the radiation belts in October 2012 might be due to radial diffusion from a dynamic outer boundary.

Fig. S1.

The energy corresponding to different values of μ (in MeV/G) along the RBSP-A orbit on October 8. The REPT instrument (30) measures electrons with energies greater than 1.8 MeV. Energies corresponding to $\mu = 3433$ MeV/G are measured by REPT nearly all the time. The (relativistic) energy for a given μ is proportional to the magnetic field strength. The thin solid lines use values from the TS04 magnetic field model. The thick dotted lines use values measured by the EMFISIS instrument on RBSP. The close agreement between the measured and TS04 model field suggest that, during this interval, the model is a reasonably accurate representation of the true geomagnetic field.

Fig. S2.

The equatorial pitch angle corresponding to different values of K (in $R_E G^{1/2}$) along the RBSP-A orbit on October 8. Large values of K correspond to small equatorial pitch angles and therefore the most field-aligned electrons. Small values of K correspond to electrons mirroring near the magnetic equator. The minimum equatorial pitch angle for a given K corresponds to locally-mirroring electrons. Electrons with $K = 0.11 R_E G^{1/2}$ have equatorial pitch angles that are generally greater than 45° and are measured nearly continuously by the REPT instrument (30).

Fig. S3.

Phase space densities based on measurements from the solid state telescope experiment on NASA's THEMIS satellite (43). Radial profiles are shown for three inbound passes of the THEMIS-A satellite on October 7 (blue), October 8 (green) and October 9 (red) for $K < 0.01 R_E G^{1/2}$ and three different values of μ . At $\mu = 100$ MeV/G the radial phase space density gradients are positive both before and during the acceleration event suggesting that, at low energies, the region outside the radiation belts ($L \gtrsim 6.5$) is a viable source of electrons. For $\mu \gtrsim 1000$ MeV/G the radial gradients both before and during the event are negative consistent with the RBSP observations of local acceleration in the heart of the radiation belts.

Fig. S4.

The intensity of VLF whistler-mode chorus waves and the flux of 2.5 MeV electrons as a function of L and Time. The power is the magnetic component of chorus waves measured by the EMFISIS instrument on RBSP-A. Chorus power is integrated from $0.1 f_{ce}$ to $0.5 f_{ce}$ where f_{ce} is the electron cyclotron frequency which captures the so-called lower-band chorus intensity which is thought to be responsible for relativistic electron acceleration (36). Chorus intensity begins to increase at the beginning of October 8 when the Dst index (figure 2) shows the onset of a geomagnetic storm and conditions favorable for whistler-mode chorus wave growth. The first period of chorus activity (in the first “dip” of the storm) is associated with a small decrease in the flux of MeV electrons. However, after a brief decrease associated with the weakening of geomagnetic activity the chorus power re-intensifies starting ~20:00 on October 8 and the MeV electron fluxes begin to intensify shortly thereafter. The correlation of chorus wave power and increases of relativistic electron flux (and phase space density) in the second period of activity is consistent with the hypothesis that chorus waves are responsible for local acceleration in the heart of the radiation belts.

Fig. S5.

Phase space density, at $\mu = 3433$ MeV/G and $K = 0.11 R_E G^{1/2}$, color-coded as a function of L^* and time for four different choices of magnetic field model. The value of L^* at a given time (and satellite position) depends significantly on the choice of model but the values of μ and K are much less sensitive to the choice in model. Importantly, the formation of peaks in phase space density is not dependent on the choice of magnetic field model although the L^* assigned to the peak does depend on the calculated value of L^* .

Fig. S6.

Phase space density plotted separately as a function of L^* and time. The green curve reproduces the curve labeled 3:32 in figure 3. It shows phase space density as a function of L^* during the time when phase space density and the geomagnetic field are undergoing the most rapid changes seen in this event. The white curve plots the same phase space density but, instead, as a function of time. The smoothness of the white curve and the presence of a spatial peak phase space density as the RBSP-A satellite moves outward toward apogee confirms the presence of a radial peak that does not depend on the value of L^* derived from a magnetic field model.

Fig. S7.

Phase space density plotted as a function of radial distance, $f(R)$ for the RBSP-B inbound pass around the time 0412 UT on October 9. While $f(R)$ is not a conserved quantity when the global magnetic field changes it still accurately represents radial gradients and allows direct comparison with the spatial scales of the RBSP orbit and electron drift shells. We have also reproduced the schematic phase space density profiles (figure 1B) to graphically illustrate our conclusion that the acceleration of relativistic electrons the October 8-9, 2012 event was produced by local acceleration through VLF wave-particle interactions.

Fig. S8.

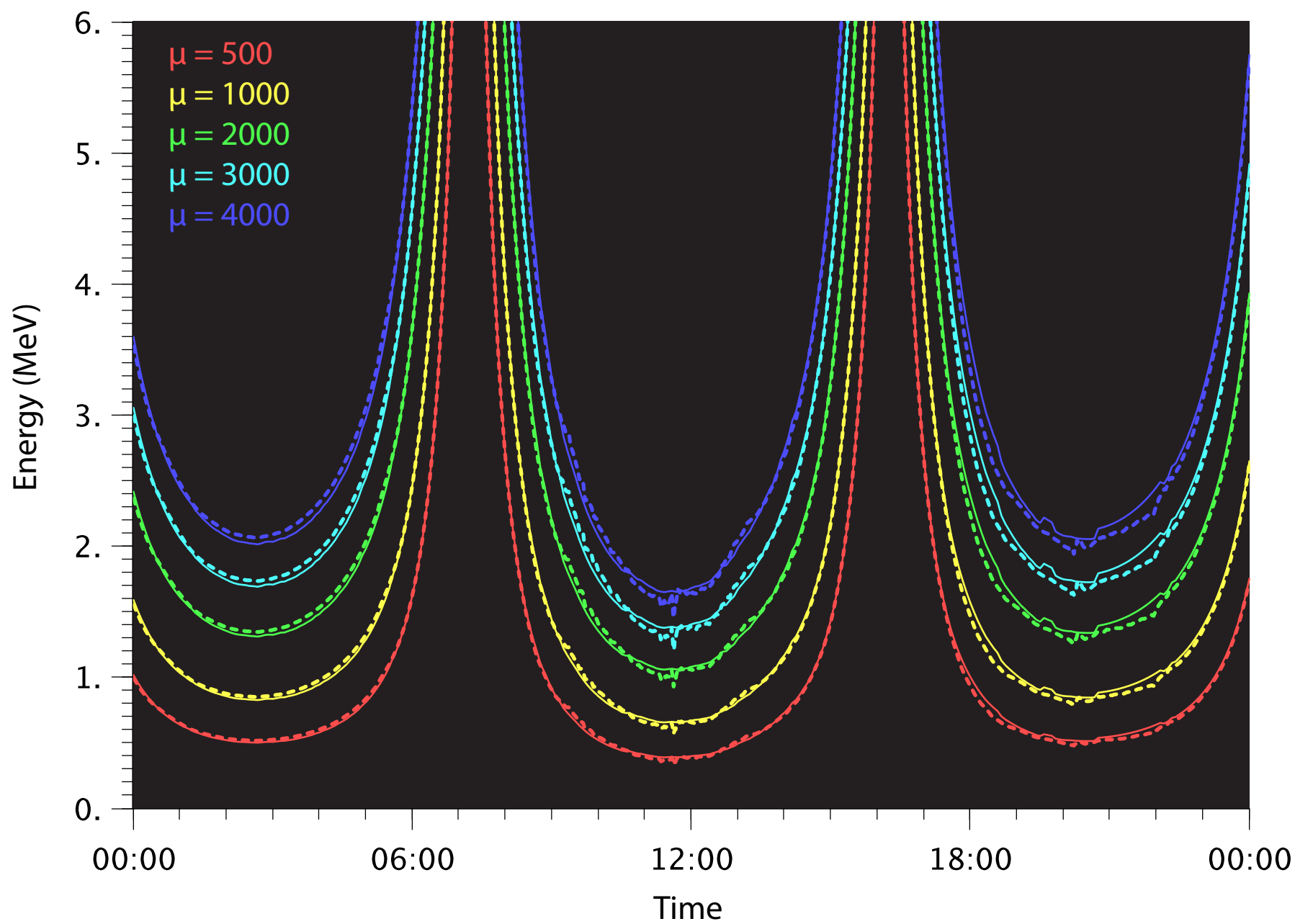
The observed magnetic field magnitude, B , is plotted against the model B from the TS04 magnetic field model. The color-coding indicated the dates. A perfect agreement between the observed and model field magnitudes would lie along the gray line of slope 1. The insert shows the distribution of samples as a function of the percent difference between the observations and the model. The slight skew to negative values indicates that, on average, the model slightly overestimates the actual field strength but overall performs remarkably well.

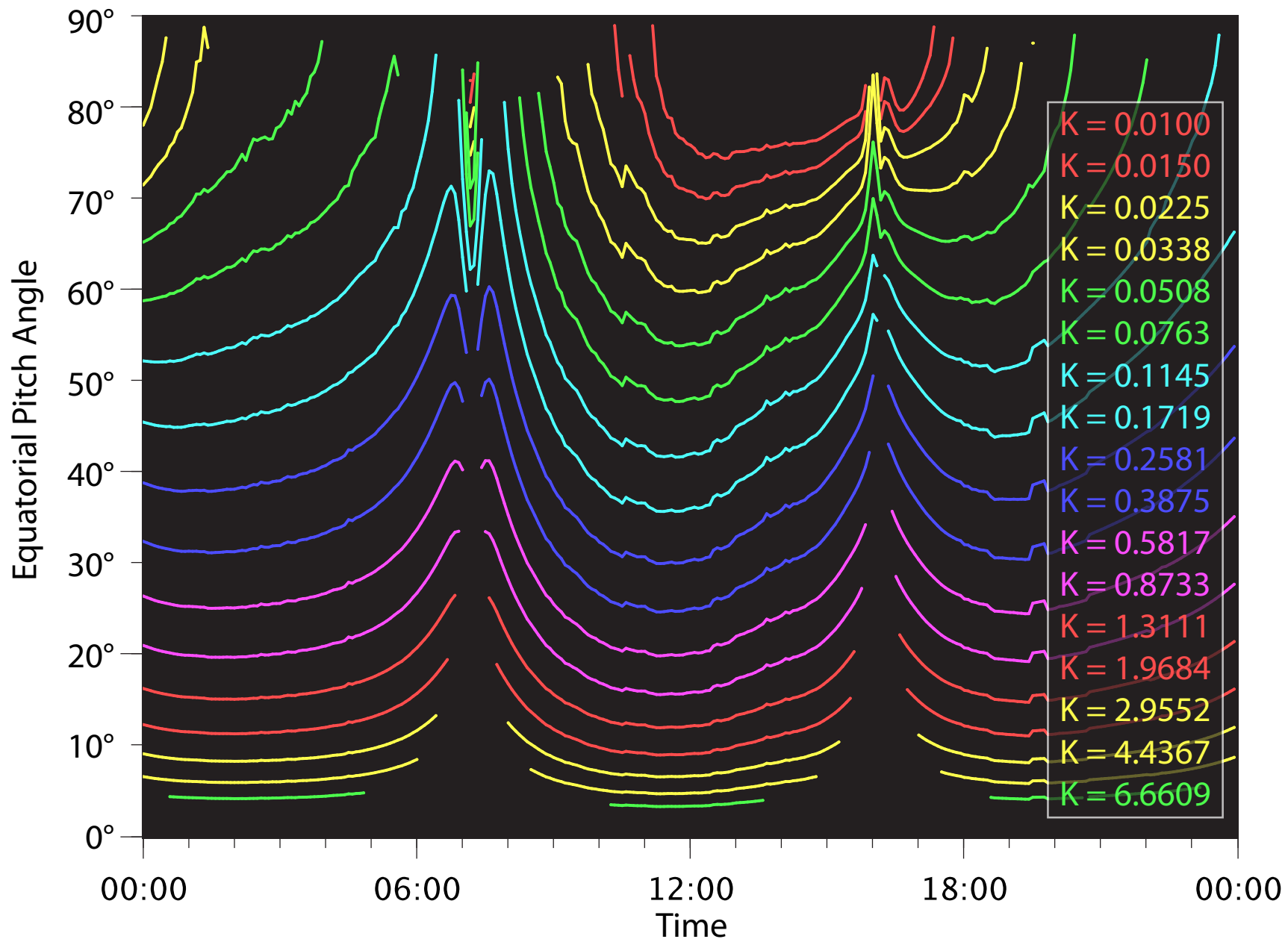
Fig. S9.

Uncertainties derived by matching phase space densities when both satellites are on the same drift shell. The difference factor is defined as the larger phase space density divided by the smaller phase space density regardless of satellite. The absolute ratios are centered around 1 indicating that neither satellite measures systematically higher fluxes (or phase space density) than the other and that, therefore, the majority of uncertainty comes from the global magnetic field model rather than instrumental cross-calibration uncertainties.

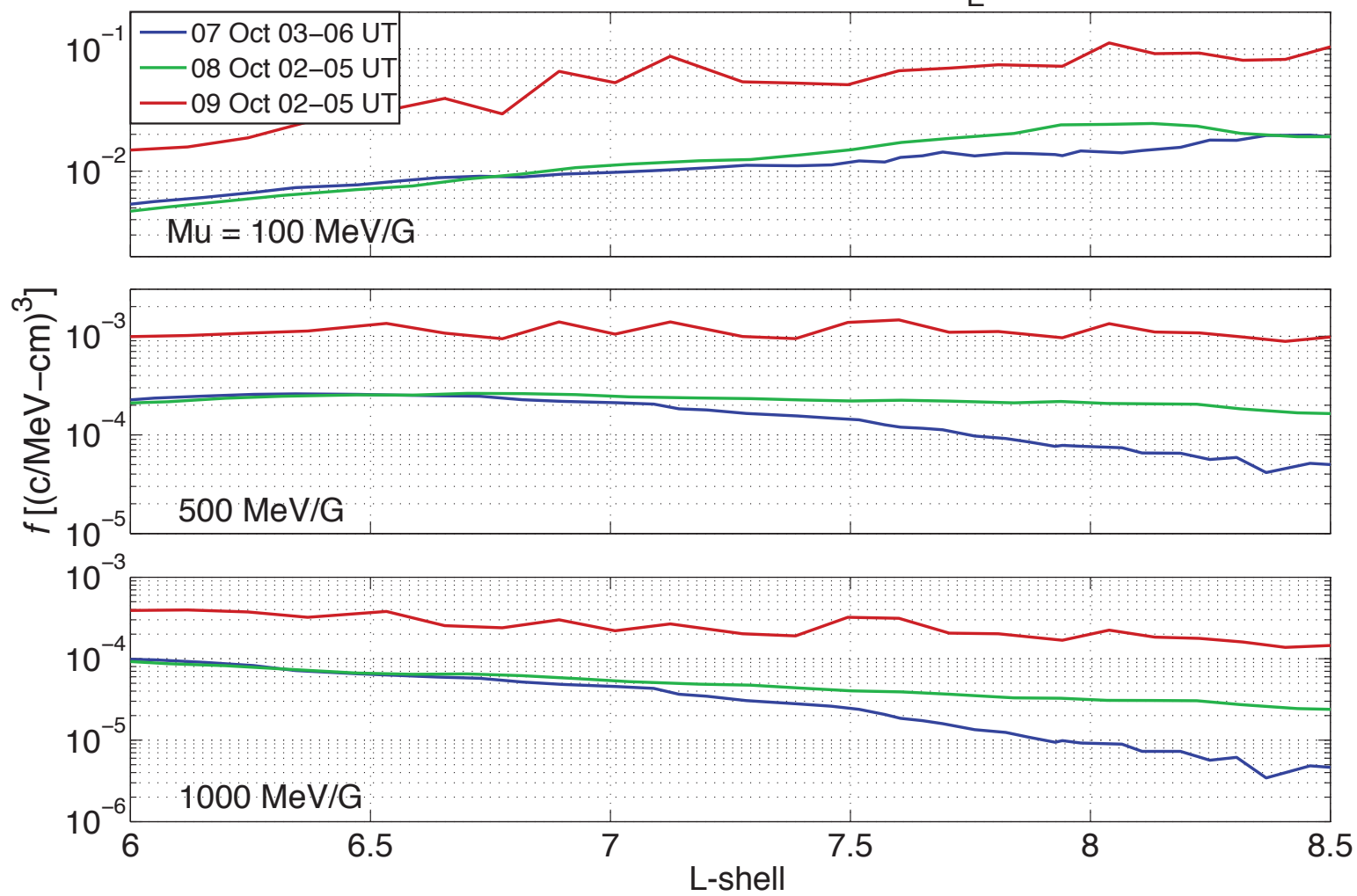
Fig. S10.

Phase space density plotted as a function of time for the two RBSP satellites and five geosynchronous satellites distributed in longitude (reference). The apogee of RBSP is at $5.7 R_E$ and geosynchronous orbit is circular at $6.6 R_E$. RBSP data are plotted for all times when $L^* > 3.8$. Geosynchronous data are plotted from all times when a reliable magnetic field direction can be obtained from the data.

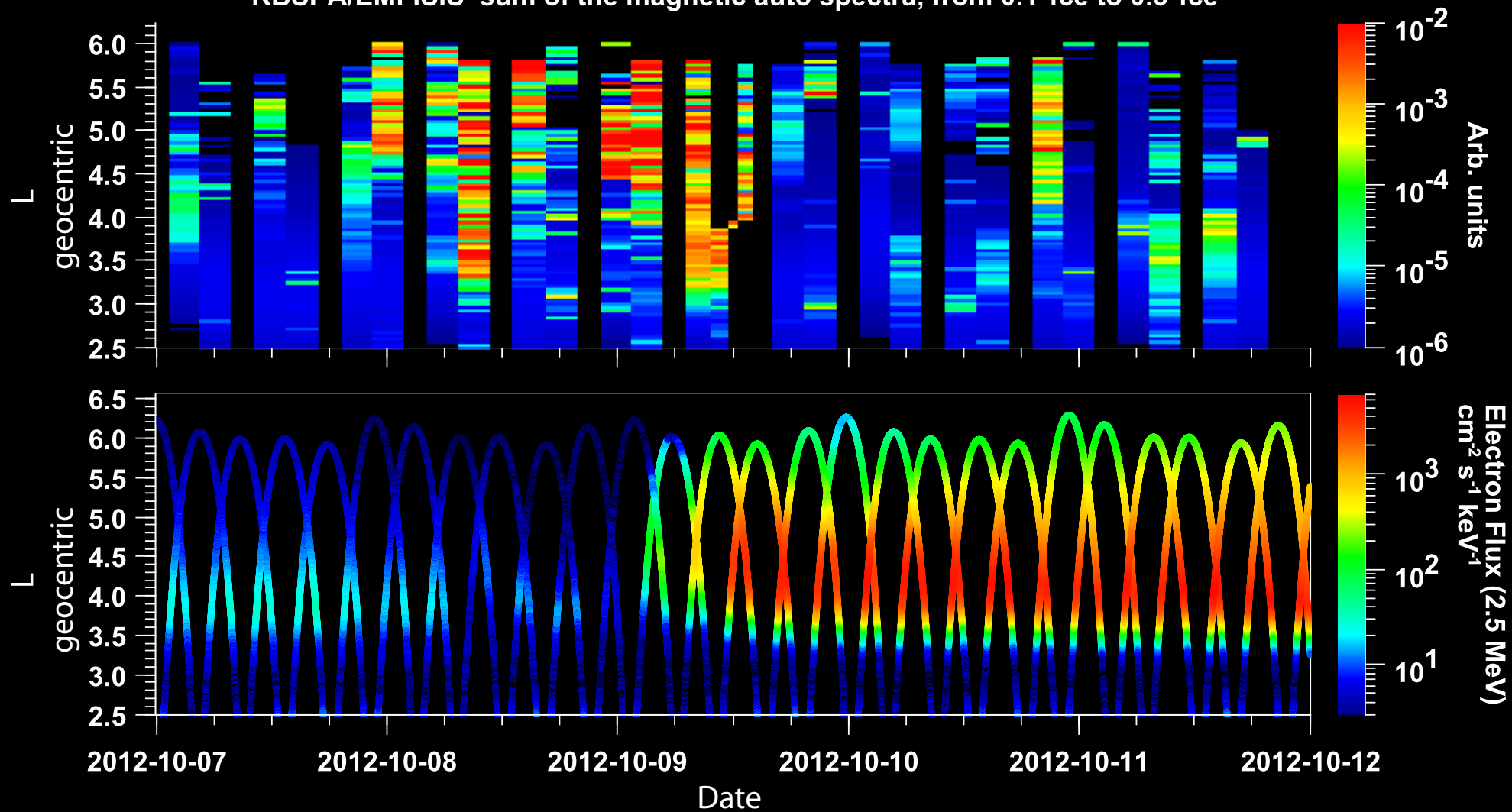


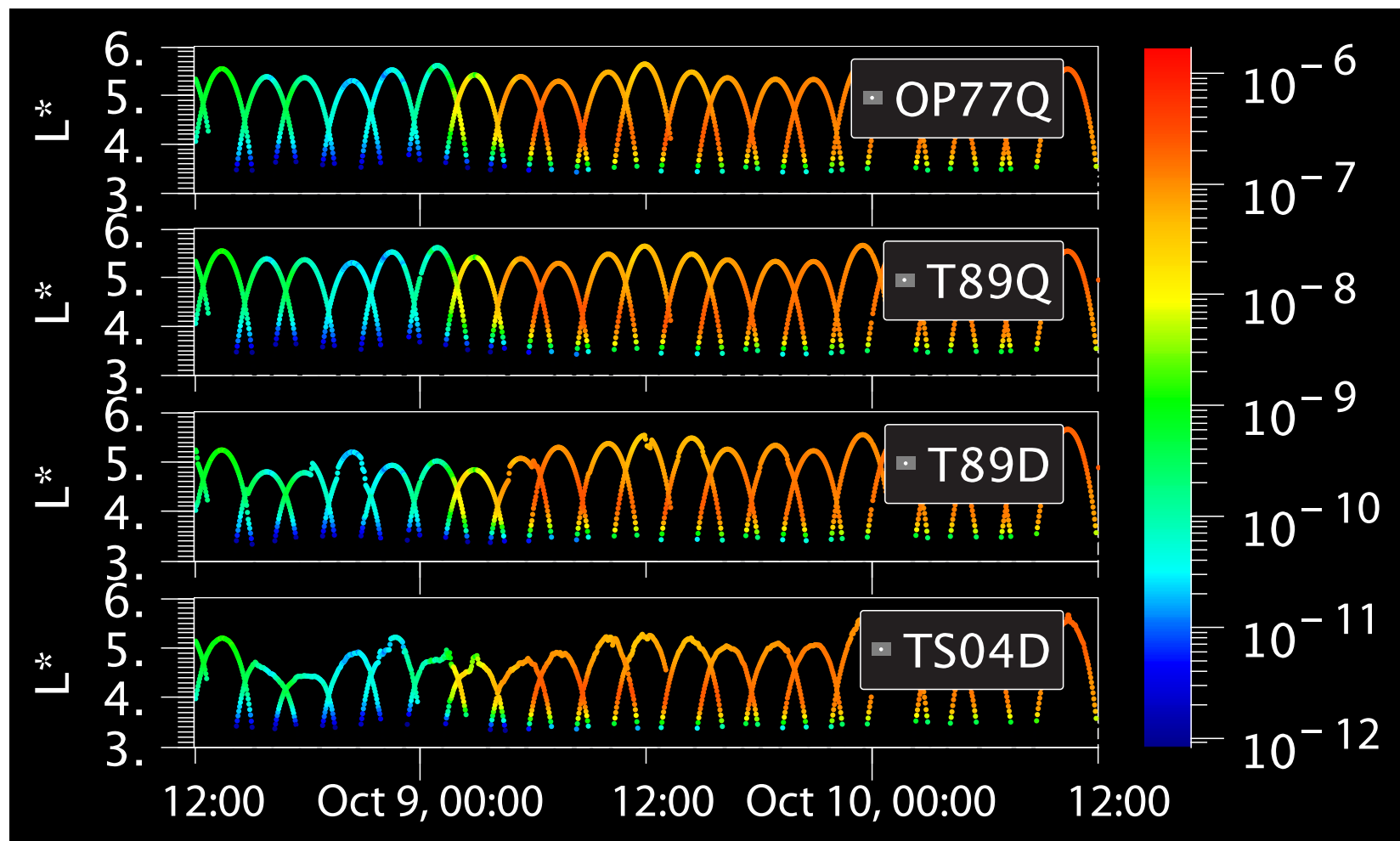


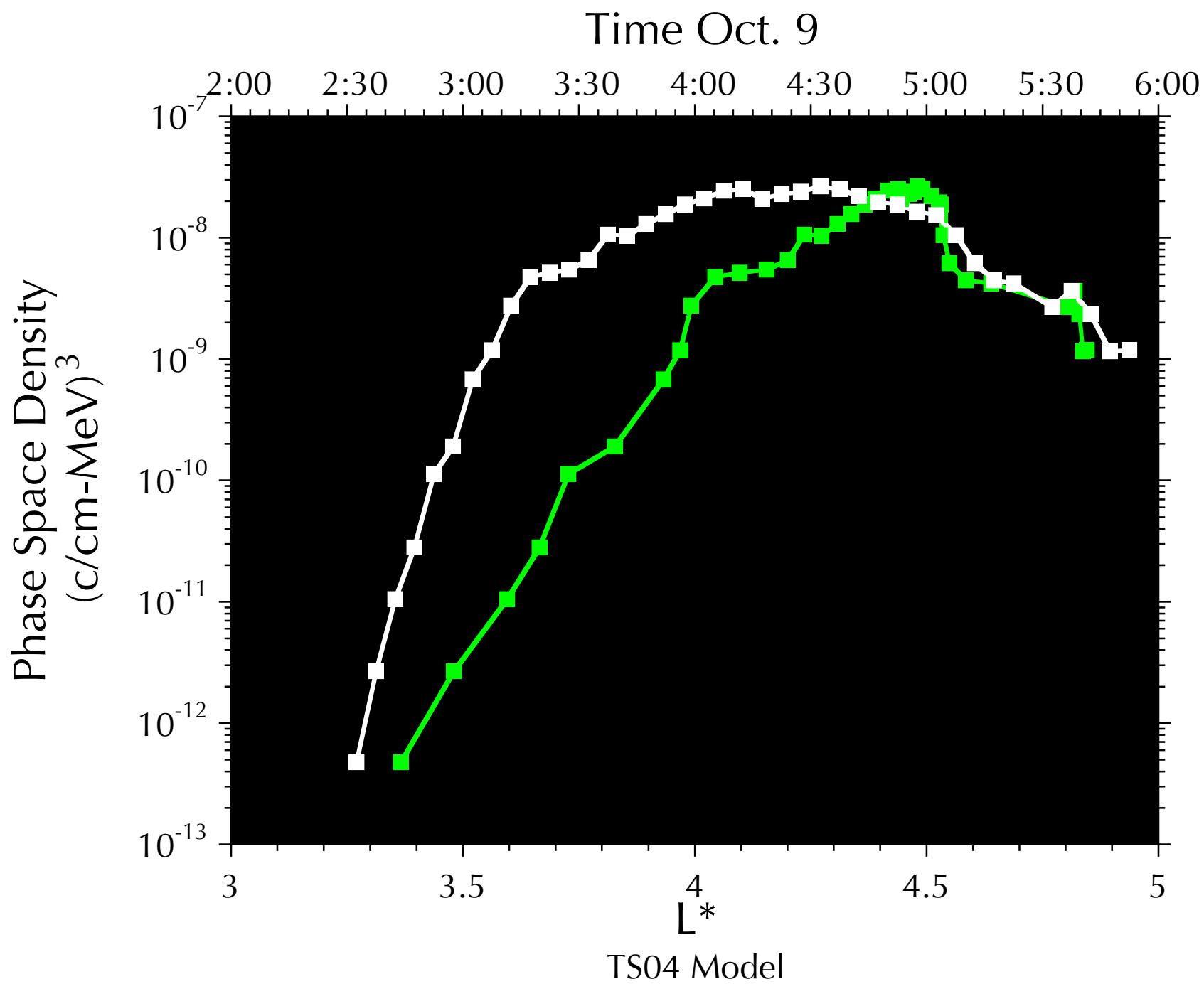
THEMIS-A Inbound ($K < 0.01 R_E G^{1/2}$)

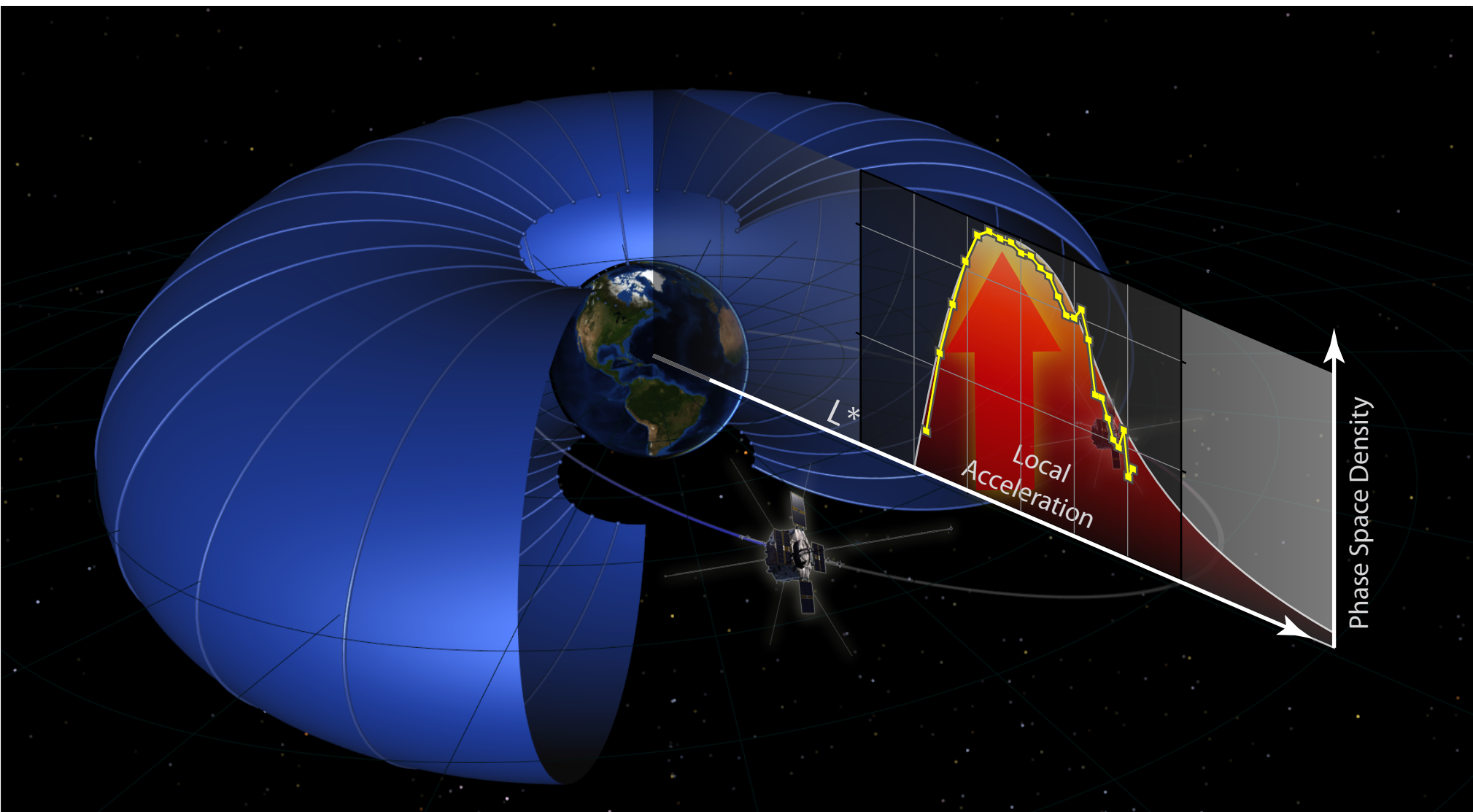


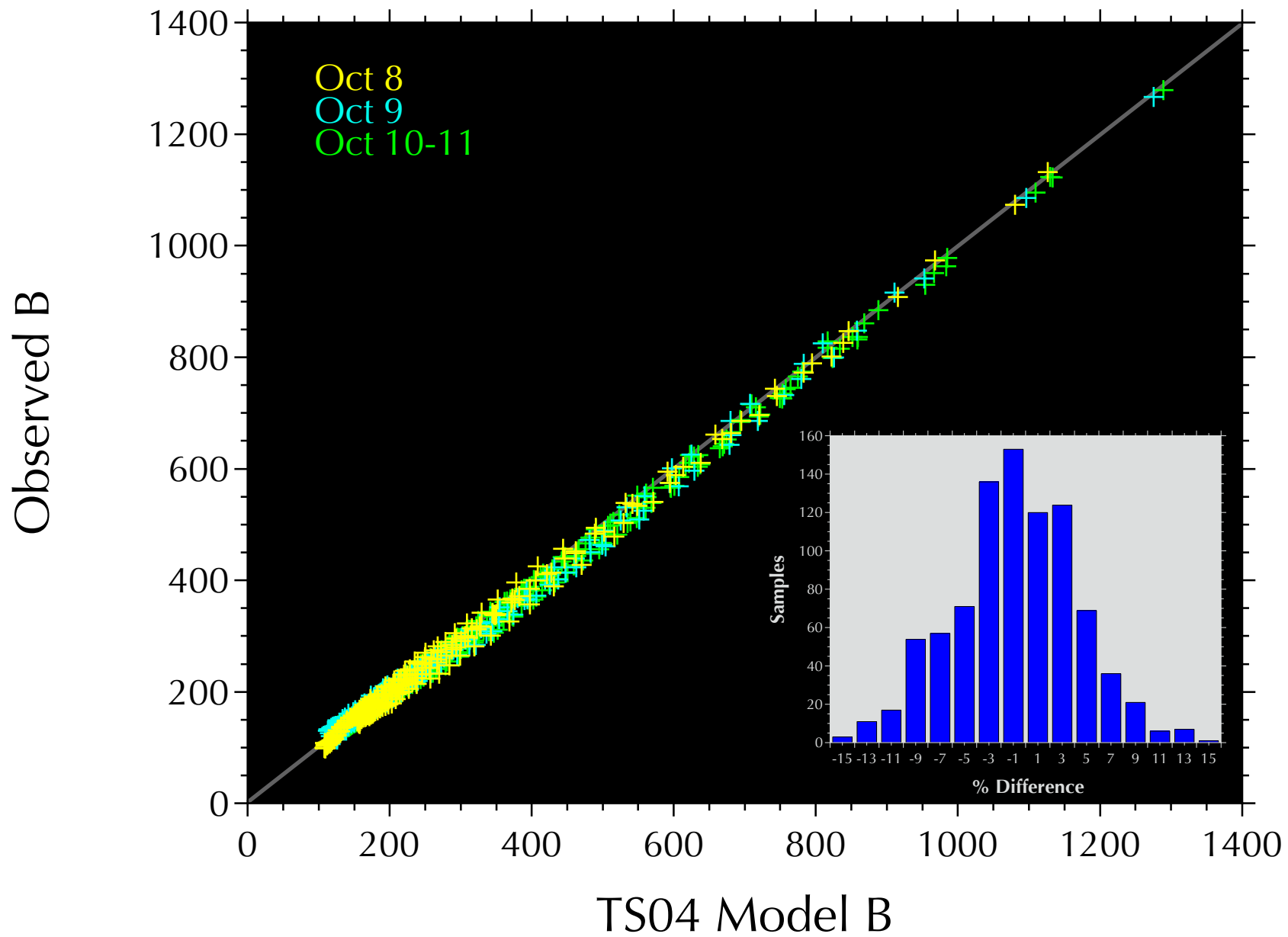
RBSPA/EMFISIS sum of the magnetic auto spectra, from $0.1 \cdot f_{ce}$ to $0.5 \cdot f_{ce}$

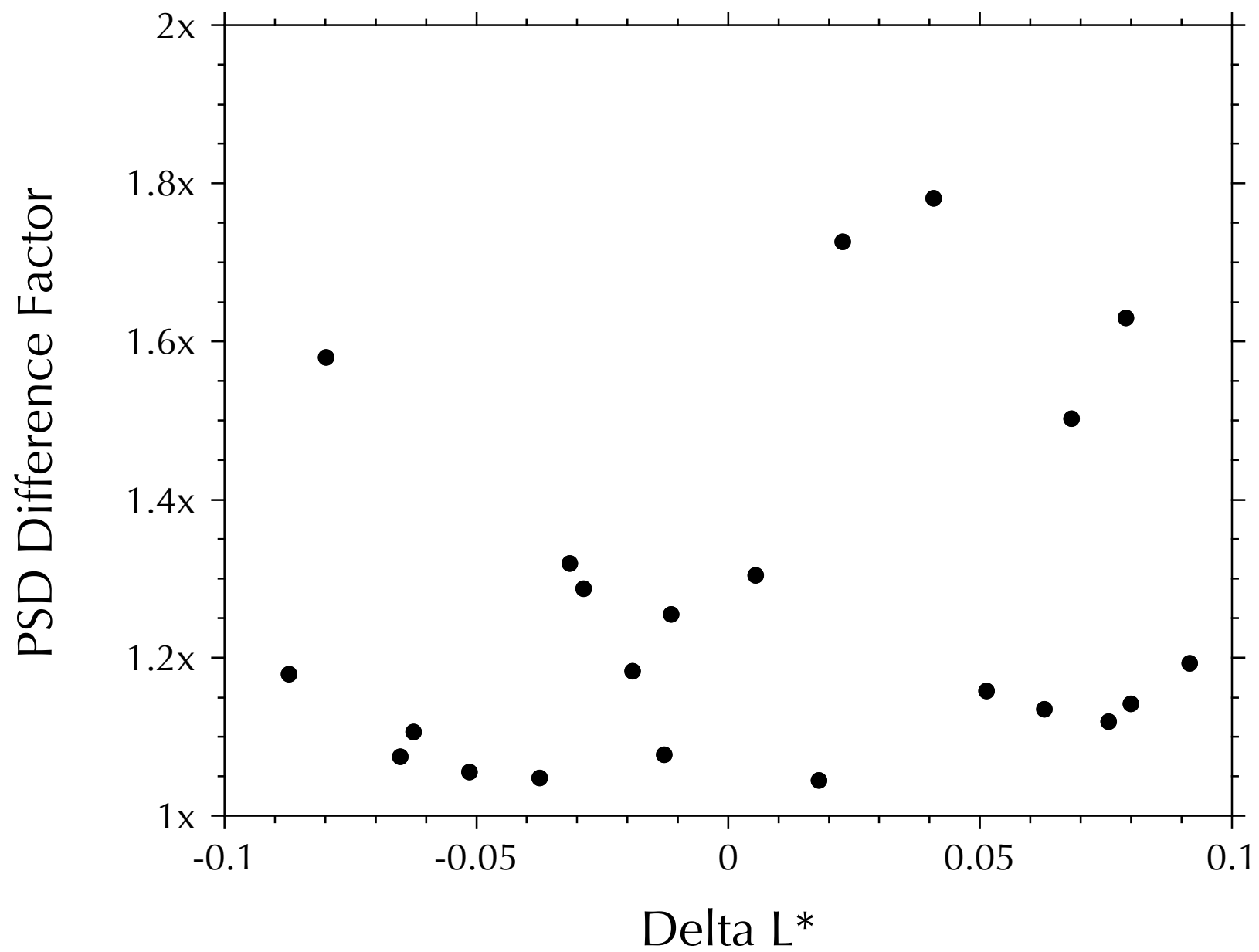


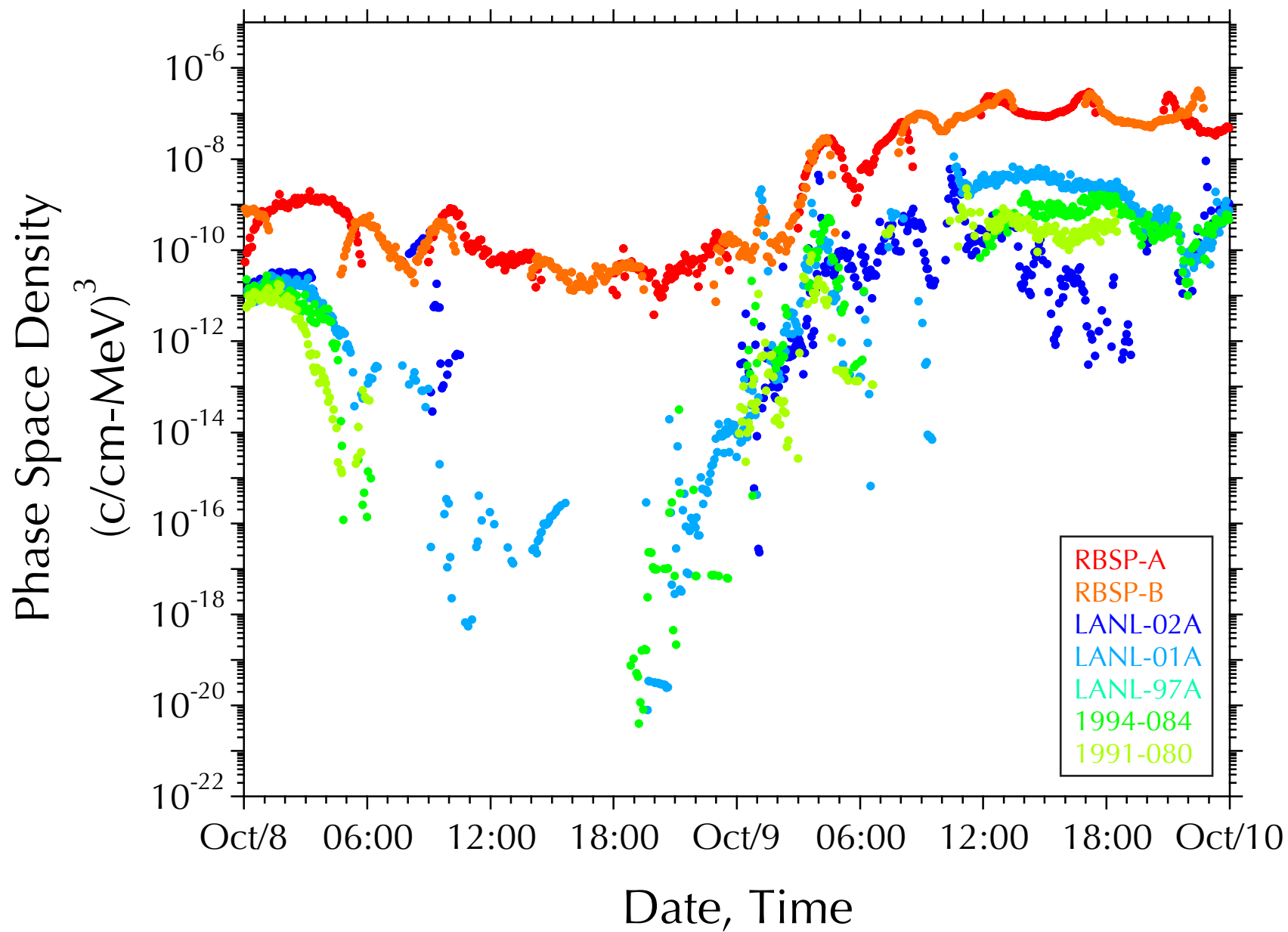












References and Notes

1. C. G. Falthammar, Effects of Time-Dependent Electric Fields on Geomagnetically Trapped Radiation. *J. Geophys. Res.* **70**, 2503–2516 (1965).
[doi:10.1029/JZ070i011p02503](https://doi.org/10.1029/JZ070i011p02503)
2. M. Schulz, L. J. Lanzerotti, *Particle Diffusion in the Radiation Belts*. (Springer-Verlag, New York, New York, 1974).
3. G. D. Reeves, D. N. Baker, R. D. Belian, J. B. Blake, T. E. Cayton, J. F. Fennell, R. H. W. Friedel, M. M. Meier, R. S. Selesnick, H. E. Spence, The global response of relativistic radiation belt electrons to the January 1997 magnetic cloud. *Geophys. Res. Lett.* **25**, 3265–3268 (1998). [doi:10.1029/98GL02509](https://doi.org/10.1029/98GL02509)
4. R. S. Selesnick, J. B. Blake, Radiation Belt Electron Observations from January 6 to 20, 1997. *Geophys. Res. Lett.* **25**, 2553 (1998). [doi:10.1029/98GL00665](https://doi.org/10.1029/98GL00665)
5. A. D. M. Walker, *Plasma waves in the magnetosphere*. (Springer-Verlag, New York, New York, 1993).
6. D. Summers, R. M. Thorne, F. Xiao, Relativistic theory of wave-particle resonant diffusion with application to electron acceleration in the magnetosphere. *J. Geophys. Res.* **103**, 20487 (1998). [doi:10.1029/98JA01740](https://doi.org/10.1029/98JA01740)
7. R. B. Horne, R. M. Thorne, Potential waves for relativistic electron scattering and stochastic acceleration during magnetic storms. *Geophys. Res. Lett.* **25**, 3011–3014 (1998). [doi:10.1029/98GL01002](https://doi.org/10.1029/98GL01002)
8. I. Roth, M. Temerin, M. K. Hudson, Resonant enhancement of relativistic electron fluxes during geomagnetically active periods. *Ann. Geophys.* **17**, 631–638 (1999).
[doi:10.1007/s00585-999-0631-2](https://doi.org/10.1007/s00585-999-0631-2)
9. D. Summers *et al.*, Model of the energization of outer-zone electrons by whistler-mode chorus during the October 9, 1990 geomagnetic storm. *Geophys. Res. Lett.* **29**, 2174 (2002). [doi:10.1029/2002GL016039](https://doi.org/10.1029/2002GL016039)
10. R. B. Horne *et al.*, Timescale for radiation belt electron acceleration by whistler mode chorus waves. *J. Geophys. Res.* **110**, A03225 (2005). [doi:10.1029/2004JA010811](https://doi.org/10.1029/2004JA010811)
11. G. Rostoker, S. Skone, D. N. Baker, On the origin of relativistic electrons in the magnetosphere associated with some geomagnetic storms. *Geophys. Res. Lett.* **25**, 3701–3704 (1998). [doi:10.1029/98GL02801](https://doi.org/10.1029/98GL02801)
12. W. W. Liu, G. Rostoker, D. N. Baker, Internal acceleration of relativistic electrons by large-amplitude ULF pulsations. *J. Geophys. Res.* **104**, 17391 (1999).
[doi:10.1029/1999JA900168](https://doi.org/10.1029/1999JA900168)
13. M. K. Hudson, S. R. Elkington, J. G. Lyon, M. Wiltberger, M. Lessard, Radiation Belt Electron Acceleration by ULF Wave Drift Resonance: Simulation of 1997 and 1998 Storms. *Space Weather* **125**, 289–296 (2001).
[doi:10.1029/GM125p0289](https://doi.org/10.1029/GM125p0289)

14. T. P. O'Brien, Energization of relativistic electrons in the presence of ULF power and MeV microbursts: Evidence for dual ULF and VLF acceleration. *J. Geophys. Res.* **108**, 1329 (2003). [doi:10.1029/2002JA009784](https://doi.org/10.1029/2002JA009784)
15. S. R. Elkington, in *Magnetospheric ULF Waves: Synthesis and New Directions*. (AGU, Washington, DC), **169**, pp. 177-193 (2006).
16. A. Y. Ukhorskiy, B. J. Anderson, K. Takahashi, N. A. Tsyganenko, Impact of ULF oscillations in solar wind dynamic pressure on the outer radiation belt electrons. *Geophys. Res. Lett.* **33**, L06111 (2006). [doi:10.1029/2005GL024380](https://doi.org/10.1029/2005GL024380)
17. R. A. Mathie, I. R. Mann, A correlation between extended intervals of ULF wave power and storm-time geosynchronous relativistic electron flux enhancements. *Geophys. Res. Lett.* **27**, 3261–3264 (2000). [doi:10.1029/2000GL003822](https://doi.org/10.1029/2000GL003822)
18. P. M. Kintner *et al.*, “The LWS Geospace Storm Investigations: Exploring the Extremes of Space Weather” (Living With A Star Geospace Mission Definition Team Report, NASA/TM-2002-211613, 2002).
19. N. P. Meredith, R. B. Horne, R. M. Thorne, R. R. Anderson, Favored regions for chorus-driven electron acceleration to relativistic energies in the Earth’s outer radiation belt. *Geophys. Res. Lett.* **30**, 1871 (2003). [doi:10.1029/2003GL017698](https://doi.org/10.1029/2003GL017698)
20. J. C. Green, M. G. Kivelson, Relativistic electrons in the outer radiation belt: Differentiating between acceleration mechanisms. *J. Geophys. Res.* **109**, A03213 (2004). [doi:10.1029/2003JA010153](https://doi.org/10.1029/2003JA010153)
21. R. H. A. Iles, N. P. Meredith, A. N. Fazakerley, R. B. Horne, Phase space density analysis of the outer radiation belt energetic electron dynamics. *J. Geophys. Res.* **111**, A03204 (2006). [doi:10.1029/2005JA011206](https://doi.org/10.1029/2005JA011206)
22. Y. Chen, G. D. Reeves, R. H. W. Friedel, The energization of relativistic electrons in the outer Van Allen radiation belt. *Nat. Phys.* **3**, 614–617 (2007). [doi:10.1038/nphys655](https://doi.org/10.1038/nphys655)
23. Y. Y. Shprits, D. A. Subbotin, N. P. Meredith, S. M. Elkington, Review of modeling of losses and sources of relativistic electrons in the outer radiation belt II: Local acceleration and loss. *J. Atmos. Sol. Terr. Phys.* **70**, 1694–1713 (2008). [doi:10.1016/j.jastp.2008.06.014](https://doi.org/10.1016/j.jastp.2008.06.014)
24. B. H. Mauk, N. J. Fox, S. G. Kanekal, R. L. Kessel, D. G. Sibeck, A. Ukhorskiy, Science Objectives and Rationale for the Radiation Belt Storm Probes Mission. *Space Sci. Rev.* (2012). [doi:10.1007/s11214-012-9908-y](https://doi.org/10.1007/s11214-012-9908-y)
25. G. D. Reeves, K. L. McAdams, R. H. W. Friedel, T. P. O'Brien, Acceleration and loss of relativistic electrons during geomagnetic storms. *Geophys. Res. Lett.* **30**, 1529 (2003). [doi:10.1029/2002GL016513](https://doi.org/10.1029/2002GL016513)
26. D. N. Baker, S. G. Kanekal, V. C. Hoxie, M. G. Henderson, X. Li, H. E. Spence, S. R. Elkington, R. H. Friedel, J. Goldstein, M. K. Hudson, G. D. Reeves, R. M. Thorne, C. A. Kletzing, S. G. Claudepierre, A long-lived relativistic electron storage ring embedded in Earth’s outer Van Allen belt. *Science* **340**, 186–190 (2013). [doi:10.1126/science.1233518](https://doi.org/10.1126/science.1233518) [Medline](#)

27. R. S. Selesnick, J. B. Blake, On the source location of radiation belt relativistic electrons. *J. Geophys. Res.* **105**, 2607 (2000). [doi:10.1029/1999JA900445](https://doi.org/10.1029/1999JA900445)
28. J. F. Fennell, J. L. Roeder, Storm time phase space density radial profiles of energetic electrons for small and large K values: SCATHA results. *J. Atmos. Sol. Terr. Phys.* **70**, 1760–1773 (2008). [doi:10.1016/j.jastp.2008.03.014](https://doi.org/10.1016/j.jastp.2008.03.014)
29. We note that at lower values of μ , corresponding to electrons in the 10s-100s keV energy range, the dynamics are dominated by processes such as enhanced convection and substorm injections that are important precursors to relativistic (MeV) electron enhancements.
30. J. B. Blake, P. A. Carranza, S. G. Claudepierre, J. H. Clemmons, W. R. Crain, Y. Dotan, J. F. Fennell, F. H. Fuentes, R. M. Galvan, J. S. George, M. G. Henderson, M. Lalic, A. Y. Lin, M. D. Looper, D. J. Mabry, J. E. Mazur, B. McCarthy, C. Q. Nguyen, T. P. O'Brien, M. A. Perez, M. T. Redding, J. L. Roeder, D. J. Salvaggio, G. A. Sorensen, H. E. Spence, S. Yi, M. P. Zakrzewski; The Magnetic Electron Ion Spectrometer, (MagEIS) Instruments Aboard the Radiation Belt Storm Probes (RBSP) Spacecraft. *Space Sci. Rev.* (2013). [doi:10.1007/s11214-013-9991-8](https://doi.org/10.1007/s11214-013-9991-8)
31. D. N. Baker, S. G. Kanekal, V. C. Hoxie, S. Batiste, M. Bolton, X. Li, S. R. Elkington, S. Monk, R. Reukauf, S. Steg, J. Westfall, C. Belting, B. Bolton, D. Braun, B. Cervelli, K. Hubbell, M. Kien, S. Knappmiller, S. Wade, B. Lamprecht, K. Stevens, J. Wallace, A. Yehle, H. E. Spence, R. Friedel, The Relativistic Electron-Proton Telescope (REPT) Instrument on Board the Radiation Belt Storm Probes (RBSP) Spacecraft: Characterization of Earth's Radiation Belt High-Energy Particle Populations. *Space Sci. Rev.* (2012). [doi:10.1007/s11214-012-9950-9](https://doi.org/10.1007/s11214-012-9950-9)
32. N. A. Tsyganenko, M. I. Sitnov, Modeling the dynamics of the inner magnetosphere during strong geomagnetic storms. *J. Geophys. Res.* **110**, A03208 (2005). [doi:10.1029/2004JA010798](https://doi.org/10.1029/2004JA010798)
33. G. A. Paulikas, J. B. Blake, Effects of the solar wind on magnetospheric dynamics: Energetic electrons at the synchronous orbit. in *Quantitative Modeling of Magnetospheric Processes* (AGU, Washington, DC) **180**, pp 180-202, (1979).
34. T. G. Northrop, E. Teller, Stability of the adiabatic motion of charged particles in the Earth's field. *Phys. Rev.* **117**, 215–225 (1960). [doi:10.1103/PhysRev.117.215](https://doi.org/10.1103/PhysRev.117.215)
35. J. G. Roederer, *Dynamics of Geomagnetically Trapped Radiation*. (Springer-Verlag, New York, 1970).
36. H. J. Kim, A. A. Chan, Fully-adiabatic changes in storm-time relativistic electron fluxes. *J. Geophys. Res.* **102**, 22 (1997). [doi:10.1029/97JA01814](https://doi.org/10.1029/97JA01814)
37. R. B. Horne, R. M. Thorne, Relativistic electron acceleration and precipitation during resonant interactions with whistler-mode chorus. *Geophys. Res. Lett.* **30**, 1527 (2003). [doi:10.1029/2003GL016973](https://doi.org/10.1029/2003GL016973)

38. Y. Miyoshi *et al.*, Rebuilding process of the outer radiation belt during the 3 November 1993 magnetic storm: NOAA and EXOS-D observations. *J. Geophys. Res.* **108**, 1004 (2003). [doi:10.1029/2001JA007542](https://doi.org/10.1029/2001JA007542)
39. R. B. Horne, R. M. Thorne, Y. Y. Shprits, N. P. Meredith, S. A. Glauert, A. J. Smith, S. G. Kanekal, D. N. Baker, M. J. Engebretson, J. L. Posch, M. Spasojevic, U. S. Inan, J. S. Pickett, P. M. Decreau, Wave acceleration of electrons in the Van Allen radiation belts. *Nature* **437**, 227–230 (2005). [doi:10.1038/nature03939](https://doi.org/10.1038/nature03939)
[Medline](#)
40. W. P. Olson, K. Pfizter, “Magnetospheric magnetic field modeling,” AFOSR-TR-77-0156, McDonnell Douglas Astronaut. Co. Huntington Beach, Calif., (1977).
41. N. A. Tsyganenko, A magnetospheric magnetic field model with a warped tail current sheet. *Planet. Space Sci.* **37**, 5–20 (1989). [doi:10.1016/0032-0633\(89\)90066-4](https://doi.org/10.1016/0032-0633(89)90066-4)
42. Y. Chen, R. H. W. Friedel, G. D. Reeves, T. G. Onsager, M. F. Thomsen, Multisatellite determination of the relativistic electron phase space density at geosynchronous orbit: Methodology and results during geomagnetically quiet times. *J. Geophys. Res.* **110**, A10210 (2005). [doi:10.1029/2004JA010895](https://doi.org/10.1029/2004JA010895)
43. Y. Chen, R. H. W. Friedel, G. D. Reeves, T. E. Cayton, R. Christensen, Multisatellite determination of the relativistic electron phase space density at geosynchronous orbit: An integrated investigation during geomagnetic storm times. *J. Geophys. Res.* **112**, A11214 (2007). [doi:10.1029/2007JA012314](https://doi.org/10.1029/2007JA012314)
44. D. L. Turner, V. Angelopoulos, Y. Shprits, A. Kellerman, P. Cruce, D. Larson, Radial distributions of equatorial phase space density for outer radiation belt electrons. *Geophys. Res. Lett.* **39**, L09101 (2012). [doi:10.1029/2012GL051722](https://doi.org/10.1029/2012GL051722)